American Mineralogist, Volume 111, pages 11–28, 2026

Complex carbonate ore mineralogy in the Mountain Pass carbonatite rare earth element deposit, U.S.A.

Kathryn E. Watts[1,*,†] and Allen K. Andersen[1]

[1]U.S. Geological Survey, 904 W. Riverside Avenue, Spokane, Washington 99201, U.S.A.

Abstract

Economic concentrations of rare earth element (REE) minerals are uncommon in the Earth's crust, with most occurring in carbonatites. Unlike most igneous rocks composed of silicate minerals, carbonatites are dominated by carbonate minerals, some of which can incorporate substantial light REEs (LREEs; La, Ce, Pr, Nd). Technological applications of REEs are numerous, and they have been identified as some of the most critical mineral commodities to the global economy. The Mountain Pass carbonatite stock in the Mojave Desert of California is the most economically significant REE deposit in the U.S.A. It contains a few to tens of percent (by volume) of the carbonate REE ore mineral bastnäsite. Despite the economic significance of the Mountain Pass deposit, studies of its ore mineralogy are limited. Here, we present new carbonate ore mineralogy data for a compositionally diverse suite of carbonatitic rocks from the Mountain Pass stock and related dikes. Whole-rock geochemical data are integrated with mineral-scale textural and chemical data obtained by scanning electron microscopy (SEM), electron probe microanalysis (EPMA), and microRaman spectroscopy. Our results document a complex spectrum of REE-bearing carbonate minerals and intermediate mixed-layer structures. Mineral species include bastnäsite [$REE(CO_3)F$], hydroxylbastnäsite [$REE(CO_3)OH$], parisite [$Ca(REE)_2(CO_3)_3F_2$], synchysite [$Ca(REE)(CO_3)_2F$], röntgenite [$Ca_2(Ce,La)_3(CO_3)_5F_3$], and sahamalite [$(Mg,Fe)(REE)_2(CO_3)_4$]. Carbonate ore mineralogy is heterogeneous within and between samples, including at the intracrystal scale. Complexly zoned crystals exhibit as many as five to six different compositional domains and syntaxial intergrowths, commonly with the more Ca-rich varieties (parisite, synchysite) forming crystal rims that surround relict bastnäsite cores. We attribute the phenocryst variability to changes in the chemistry and temperature of primary carbonatite magmas and evolved/exsolved fluids. Cross-cutting vein textures of calcite, celestine and various REE carbonate minerals, breccia blocks lined by fine-grained bastnäsite, and the presence of hydroxylbastnäsite and partially hydroxylated bastnäsite point to the role of secondary hydrothermal processes in REE mineralization. Fluorcarbonate mineral compositions demonstrate that La and Ce are more structurally abundant in bastnäsite, whereas parisite and synchysite contain a greater proportion of REE heavier than Pr (Nd, Sm, Eu, Gd) and Y. Atomic ratios of Pr/(Nd+Pr) are likewise variable, with the highest average value for bastnäsite (0.25) compared to parisite (0.22) and synchysite (0.21). This finding has geometallurgical implications, given that current mining operations are focused on recovering Nd and Pr for high field strength permanent magnets, and the Nd/Pr ratios are a critical factor in ore processing and magnet manufacture.

Keywords: Carbonatite, rare earth elements, critical minerals, fluorcarbonate, bastnäsite, hydroxylbastnäsite, parisite, synchysite, röntgenite, sahamalite

Introduction

Carbonatites and the carbonate minerals they contain are the main hosts of economic rare earth element (REE) deposits on Earth. Many technological applications and innovations are dependent on REEs, and securing these critical mineral commodities is necessary for national security (Nassar and Fortier 2021). Ore deposit models require understanding the formation of carbonatites and the processes by which REEs are concentrated in geologically rare carbonate minerals, such as bastnäsite. Though carbonatites are found on every continent and range in age from Precambrian to Quaternary (Liu et al. 2023a), relatively few possess economic REE mineralization. The largest active mines for carbonatite REE deposits are located in China (Bayan Obo, Maoniuping, Dalucao, Muluozhai, Yangfang), Brazil (Araxá), Australia (Mount Weld), and the United States (Mountain Pass) (Liu et al. 2023b). Advanced mining projects are ongoing for dozens of carbonatite occurrences globally.

The Mountain Pass carbonatite stock is one intrusive body within a suite of Mesoproterozoic (ca. 1.4 Ga), REE-rich carbonatite and alkaline silicate intrusions in the Mojave Desert of southeastern California (Fig. 1a; Castor 2008; Poletti et al. 2016; Watts et al. 2022, 2024; Benson and Watts 2024; Benson et al. 2025). The carbonatite stock (referred to as the Sulphide Queen stock) is the only known intrusion of sufficient size and grade to mine. However, dozens of REE-rich carbonatite dikes

* Corresponding author E-mail: kwatts@usgs.gov Orcid https://orcid.org/0000-0002-6110-7499

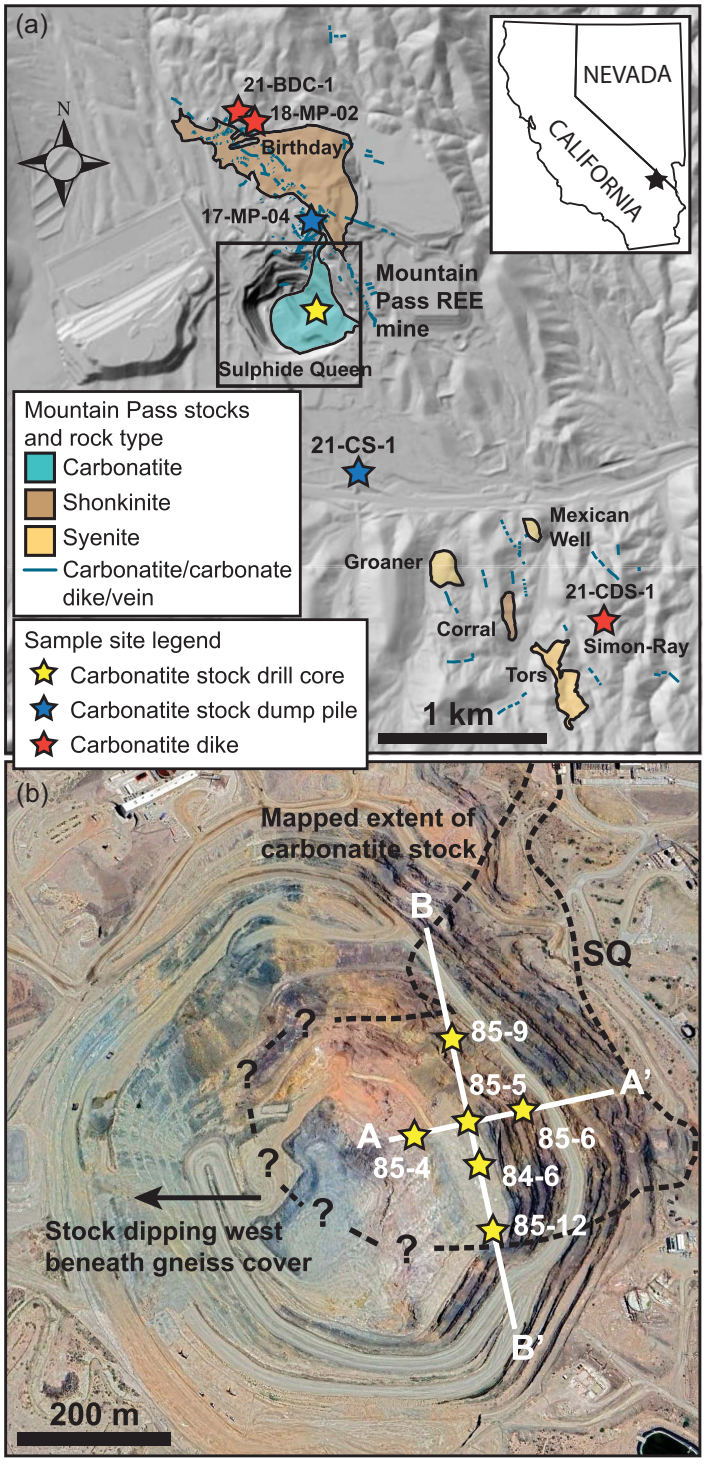

Figure 1. (**a**) Location map of the Mountain Pass REE mine in southeastern California, showing carbonatite and alkaline stocks, carbonatite dikes and carbonate veins, and sampling localities. Digital elevation basemap from USGS National Map 3D Elevation Program (3DEP; USGS 2025). (**b**) Plan view of drill core sample locations in the Sulphide Queen (SQ) carbonatite stock, overlain on Google Earth satellite imagery (accessed 2025) of the Mountain Pass mine pit. White lines show locations of geologic cross sections in (**c**) and (**d**). (**c**) West-to-east (A-A′) and (**d**) north-to-south (B-B′) geologic cross sections through the carbonatite stock, showing lithological variation, drill hole locations, and drill core sample locations [cross sections modified after Castor (2008)]. The elevation surface of the bottom of the pit at the time of Castor's mapping in the 1980s was ~1420 m (4670 ft), indicated by the thin horizontal black lines near the top of the cross sections. Most of the geology shown in these cross sections has been mined out. The elevation surface of the bottom of the pit is now below 1340 m (4400 ft). Reference depth markers are shown for approximately 1400 m (4600 ft), 1370 m (4500 ft), and 1340 m (4400 ft) in each cross section.

and carbonate veins are present north and south of the mine (Fig. 1a). A small open pit (currently ~750 m by ~870 m wide and ~200 m deep) marks the location of the Mountain Pass mine, which has been in operation since the 1950s, shortly after the deposit's discovery (Olson et al. 1954) (Fig. 1b). Carbonatites of the Mountain Pass deposit have a higher average REE grade (~8–9 wt% total rare earth oxides, TREO) compared to the Chinese Bayan Obo and Maoniuping deposits (~3–6 wt% TREO) (Verplanck et al. 2016; Liu et al. 2023b). Locally, Mountain Pass carbonatites have extreme values of ~15–25 wt% TREO (Castor 2008). The composite carbonatite stock is mineralogically and texturally diverse, with calcite- and dolomite-dominant intercalated intrusions bordered by breccia zones (Figs. 1c–1d).

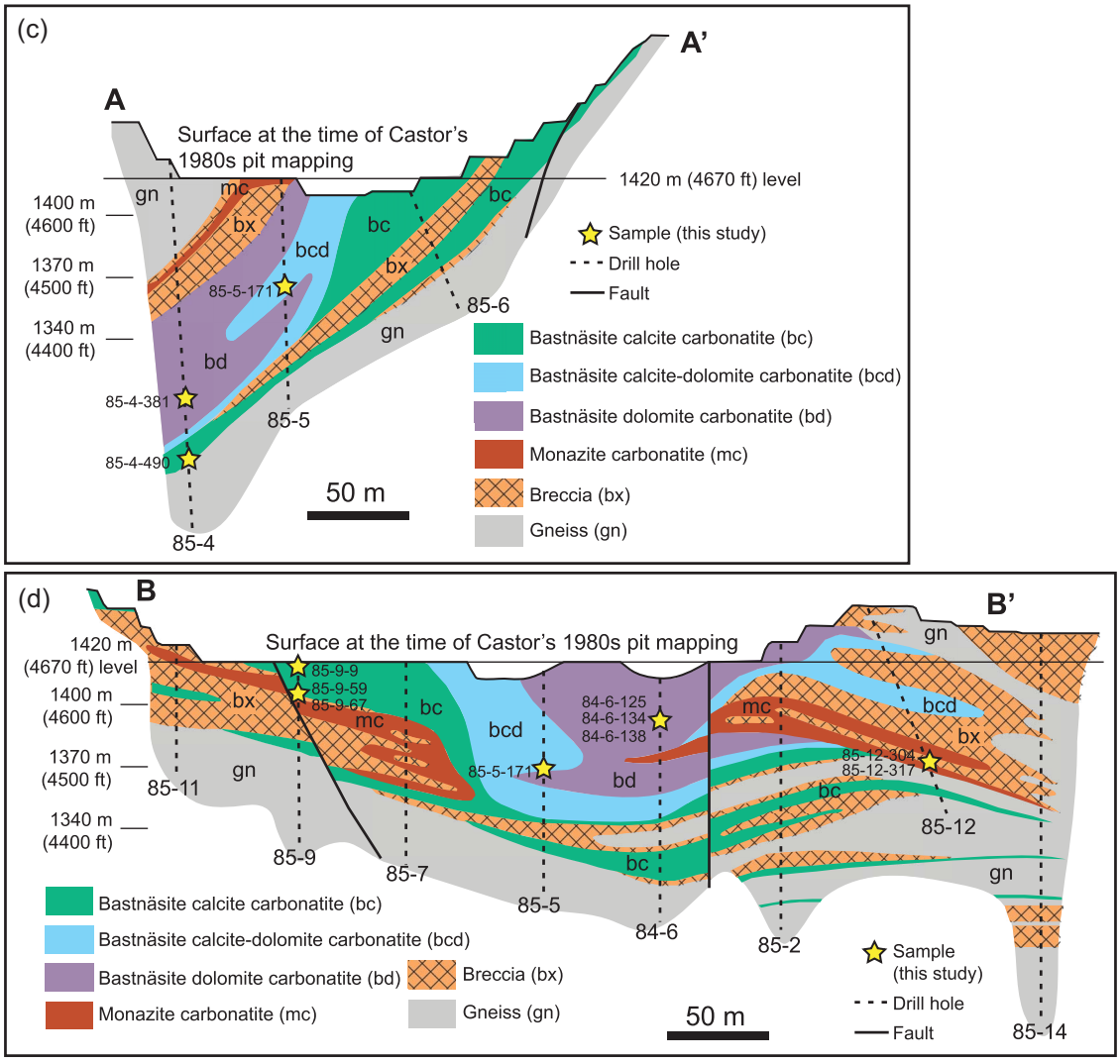

Figure 1. (*Continued*)

Bastnäsite, a fluorcarbonate mineral that incorporates REEs in its structure [REE(CO_3)F], predominantly the light REEs (LREEs; La, Ce, Pr, Nd), is the main ore mineral in Mountain Pass carbonatite (Olson et al. 1954; Castor 2008). In a few parts of the stock, monazite [REE(PO_4)] is the dominant REE mineral (Figs. 1c–1d), but in general, the carbonatite is phosphorus-poor and lacks phosphate minerals like apatite and monazite (Benson and Watts 2024). Although other REE-bearing carbonate minerals have been reported in Mountain Pass ore rocks, such as synchysite and parisite (Castor 2008) and sahamalite (Jaffe et al. 1953), high spatial resolution studies of their textural contexts and chemical compositions are lacking. Here we provide whole-rock and mineral-scale textural and chemical data for a compositionally diverse suite of carbonatites and carbonate ore minerals. The new data allow us to describe several distinct REE (±Ca, Mg, Fe, F, OH)-bearing carbonate species and to investigate igneous and hydrothermal mineralization processes in the Mountain Pass REE deposit.

Samples and Methods

Carbonatite rock samples were collected from the stock (location of the mine pit) and dikes to the north and south of the mine (Fig. 1a). Stock samples include pit, drill core, and dump samples of the carbonatite ore body and historical drill core, represented in N-S and W-E transects across the ore body (Figs. 1b–1d). Dike samples were collected near the Birthday discovery site, ~1 km north of the stock, and at the Simon-Ray prospect, ~2.5 km southeast of the stock (Fig. 1a). Hereafter, these sample groups are referred to as "stock" and "dike." Stock samples typically have large pink and white-gray baryte phenocrysts set in a matrix of white and tan calcite, brown dolomite, and interstitial pale tan bastnäsite (Figs. 2a–2c). Individual crystals of bastnäsite are usually too fine-grained to see with the naked eye, but massive bastnäsite can be distinguished by the color variation in the groundmass (e.g., pale tan-yellow matrix material in Fig. 2b). Conversely, dike samples often have conspicuous, tabular laths of pale tan-pink bastnäsite phenocrysts that are easily seen (Figs. 2d–2f). In some cases, bastnäsite demonstrates positive relief from the groundmass due to differential weathering (e.g., Fig. 2e), and extremely coarse bastnasite textures, with crystals ~4–6 cm long, are present locally (e.g., Fig. 2f). In petrographic examination of polished thin sections, it is apparent that bastnäsite crystals are high relief in plane-polarized light, ranging from pale tan to dark brown, and some phenocrysts display pleochroism in shades of pink, purple, tan, yellow, and green (Fig. 3a). Bastnäsite crystals have strong birefringence, with third order and higher interference colors in cross-polarized light (Fig. 3b). In stock samples, bastnäsite typically occurs as small (<300 μm), subhedral, interstitial

grains that surround large (>0.5 mm) calcite and baryte phenocrysts (Figs. 3c–3d). Veins and veinlets of bastnäsite and other REE carbonate minerals are observed to crosscut baryte phenocrysts and other major rock-forming minerals (Fig. 3e). In dike samples, bastnäsite occurs as large phenocrystic laths (most ~0.25–1 cm long; in extreme examples >5 cm long) and subhedral crystals in the groundmass intergrown with fine- to coarse-grained calcite and baryte (Fig. 3f).

Whole-rock geochemistry was acquired for carbonatite rock samples at AGAT Laboratories in Calgary, Canada, under contract to the U.S. Geological Survey (USGS). All samples were powdered to <75 µm and digested in hydrochloric, nitric, hydrofluoric, and perchloric acids to ensure REE-bearing refractory minerals were fully dissolved. Carbonate carbon was analyzed using a dilute perchloric acid digestion to release inorganic carbon as CO_2, which was then measured by infrared detection. Sulfur was measured by combustion in an induction furnace and with a solid-state infrared detector. Fluorine was determined by ion-selective electrode (ISE) after metal ion-fluoride complexes were dissociated in an ammonium nitrate solution. After drying and removal of hygroscopic water, essential water was measured by heating the sample in a tube furnace and absorbing expelled water with magnesium perchlorate. Major element oxides were measured by wavelength dispersive X-ray fluorescence spectrometry (WDXRF), trace elements were measured by inductively coupled plasma-optical emission spectroscopy (ICPOES), and REE were measured by inductively coupled plasma mass spectrometry (ICPMS) for high-concentration REE samples (>1000 ppm total REE).

Mineral-scale geochemical data were collected for REE-bearing carbonates in polished thin sections using a scanning electron microscope (SEM) and an electron probe micro analyzer (EPMA) at USGS laboratories in Menlo Park, California, and Lakewood, Colorado. A Tescan VEGA3 SEM instrument, equipped with Oxford X-MaxN energy-dispersive spectrometers, was used in conjunction with Oxford AZtec 6.0 software to create mosaic layered elemental maps of thin sections. Mosaic elemental maps were constructed from SEM energy dispersive spectra (EDS) collected at an accelerating voltage of 20 kV, beam current of 16 nA, pixel dwell time of 35 µs, and a magnification of 200×. Chemical analyses of REE-bearing carbonate mineral phases were acquired with a JEOL 8530F Plus EPMA instrument, using an accelerating voltage of 10 kV, a current of 20 nA, and a 5 µm beam diameter. See Table 1 for a compilation of EPMA acquisition parameters. A modeled, mean atomic number (MAN) background correction was used, and interference corrections were applied using Probe for EPMA 13.9.1 software with an iterated matrix-corrected interference correction procedure (Donovan et al. 1993, 2016, 2021).

Chemical data acquired by EPMA were used to calculate mineral formulas for each analytical spot, normalized to a total positive charge for each species as follows: +3 for bastnäsite [$REE(CO_3)F$], +5 for synchysite [$Ca(REE)(CO_3)_2F$], +8 for parisite [$Ca(REE)_2(CO_3)_3F_2$] and sahamalite [$(Mg,Fe)(REE)_2(CO_3)_4$], +11 for B_2S [$Ca(REE)_3(CO_3)_4F_3$], +13 for röntgenite [$Ca_2(REE)_3(CO_3)_5F_3$], and +19 for B_3S_2 [$Ca_2(REE)_5(CO_3)_7F_5$], with *B* (bastnäsite) and *S* (synchysite) used to describe mixed-layer structures (see Table 2 for mineral and mixed-layer formulas and Fig. 4 for illustrations of structures). Carbonate (CO_3^{2-}) content was calculated by balance with the number of cations per formula unit, and OH^- content was calculated by charge difference where there was a F^- deficit, detected only for bastnäsite, which is consistent with the known hydroxylated variety of this fluorcarbonate (hydroxylbastnäsite).

The presence of OH^- in bastnäsite-hydroxylbastnäsite from four samples was verified by microRaman spectroscopy. Raman spectra were collected at ambient temperature using a Thermo DXR Raman microscope with a 532 nm (green) laser and an extended-range grating, which allowed the collection of data over the wavenumber range of 200 to 6000 cm^{-1} Raman shifted units (rsu), partially covering the energy range of REE luminescence. The extended-range grating, with a manufacturer-stated resolution of ±10 cm^{-1}, allowed the collection of element-specific photoluminescence spectral features, as well as the full range of OH^-/H_2O Raman-active bands. Acquisition was performed in point map mode using Thermo Fisher Scientific OMNIC and Atlus software (both version 9.12.928) for spectral collection and mapping. Laser power was held constant at 4 mW, and spot size was reduced to ~3 µm in diameter using a 100× objective and 25 µm pinhole aperture. Exposure times were 5 and 9 s, and the number of exposures ranged from 10 to 20.

Results

Carbonatite Whole-Rock Chemistry

Carbonatite samples typically have ~10–40 wt% CaO, ~1–12 wt% MgO, and <4 wt% Fe_2O_3 (Table 3). When plotted in normalized $CaO+MgO+Fe_2O_3$ ternary space, the carbonatite samples span the calcite and calcite-dolomite compositional fields, with the exception of one highly silicified sample (42 wt% SiO_2) that plots in the ankerite field (Fig. 5a). Relatively high SiO_2 contents (>5 wt%) are present in four other carbonatite samples, attributed to silicification. Whole-rock S contents span ~1–8 wt%, F contents ~0.1–2.1 wt%, and H_2O contents ~0.5–1.1 wt% (Table 3). Phosphorus concentrations are low, mostly <1 wt% P_2O_5. Phenocrystic baryte with celestine alteration and crosscutting celestine veins impart whole-rocks with high concentrations of BaO (~5–30 wt%) and SrO (~1–15 wt%) (e.g., Fig. 6a). Mountain Pass carbonatites have distinctly high concentrations of Th (~50–3000 ppm) and Pb (~50–5000 ppm), owing to the presence of Th-bearing (bastnäsite, monazite, thorite) and Pb-bearing (galena) minerals and mineral inclusions (e.g., Figs. 6a–6b).

Concentrations of REEs span about two orders of magnitude for the Mountain Pass carbonatite samples, with the highest concentrations of LREE (7.6 wt% La, 10.8 wt% Ce, 0.8 wt% Pr, 2.5 wt% Nd) at about 50 000–100 000 × chondrite values (Fig. 5b; Table 3). Chondrite-normalized carbonatite REE patterns are characterized by a negative slope in which REE concentrations progressively decrease with increasing atomic number, such that concentrations of the heaviest REE (Yb, Lu) are not substantially elevated above typical crustal rocks (Fig. 5b). This characteristic negative-sloping REE pattern is typical of carbonatites globally (e.g., Hornig-Kjarsgaard 1998; Verplanck et al. 2016) and is similar to the alkaline silicate rocks of the Mountain Pass intrusive suite, though those rocks do not reach ore-grade concentrations of LREE (Fig. 5b). Compared to the stock, carbonatite dikes at Mountain Pass have distinctly higher concentrations of mid-atomic number REE (MREE; Sm, Eu, Gd) and heavy REE (HREE; Tb, Dy, Ho, Er, Tm, Yb, Lu) (Fig. 5b; Table 3), attributed to the greater proportion of Ca-bearing REE carbonate minerals in the dike samples, which incorporate more MREE and HREE than bastnäsite (see subsequent section on REE carbonate mineral chemistry).

Textures of REE Carbonate Ore Minerals

Detailed pit mapping indicates the stock is an amalgamation of discrete carbonatite intrusions with different physical and chemical characteristics, represented in a series of intercalated sills, pods, dikes, lenses, and breccias (Castor 2008; Figs. 1c–1d). Bastnäsite in the stock is typically interstitial and intergrown with matrix calcite surrounding large baryte phenocrysts (Fig. 6a). In contrast, carbonatite dikes to the north and south of the stock have a porphyritic texture with bastnäsite as the main phenocryst mineral (Figs. 6b–6c). In the dikes, bastnäsite is rimmed by Ca-rich fluorcarbonate phases. The rims are chiefly composed of parisite, but also contain syntaxial intergrowths of synchysite, B_2S, B_3S_2, and rare röntgenite. (Figs. 6b and 7a–7d). In some dikes, Ca-REE fluorcarbonates appear to have fully or nearly fully replaced original bastnäsite, with only sparse, patchy bastnäsite cores remaining (Figs. 6c and 7a). Bastnäsite phenocrysts in the dikes have pervasive cracks and fractures, commonly filled by calcite, baryte, and celestine (Figs. 6b, 6c, and 6g).

In the carbonatite stock, fine-grained bastnäsite crystals line the margins of baryte, calcite, and dolomite phenocrysts (Fig. 6d), and REE-bearing carbonate minerals crosscut

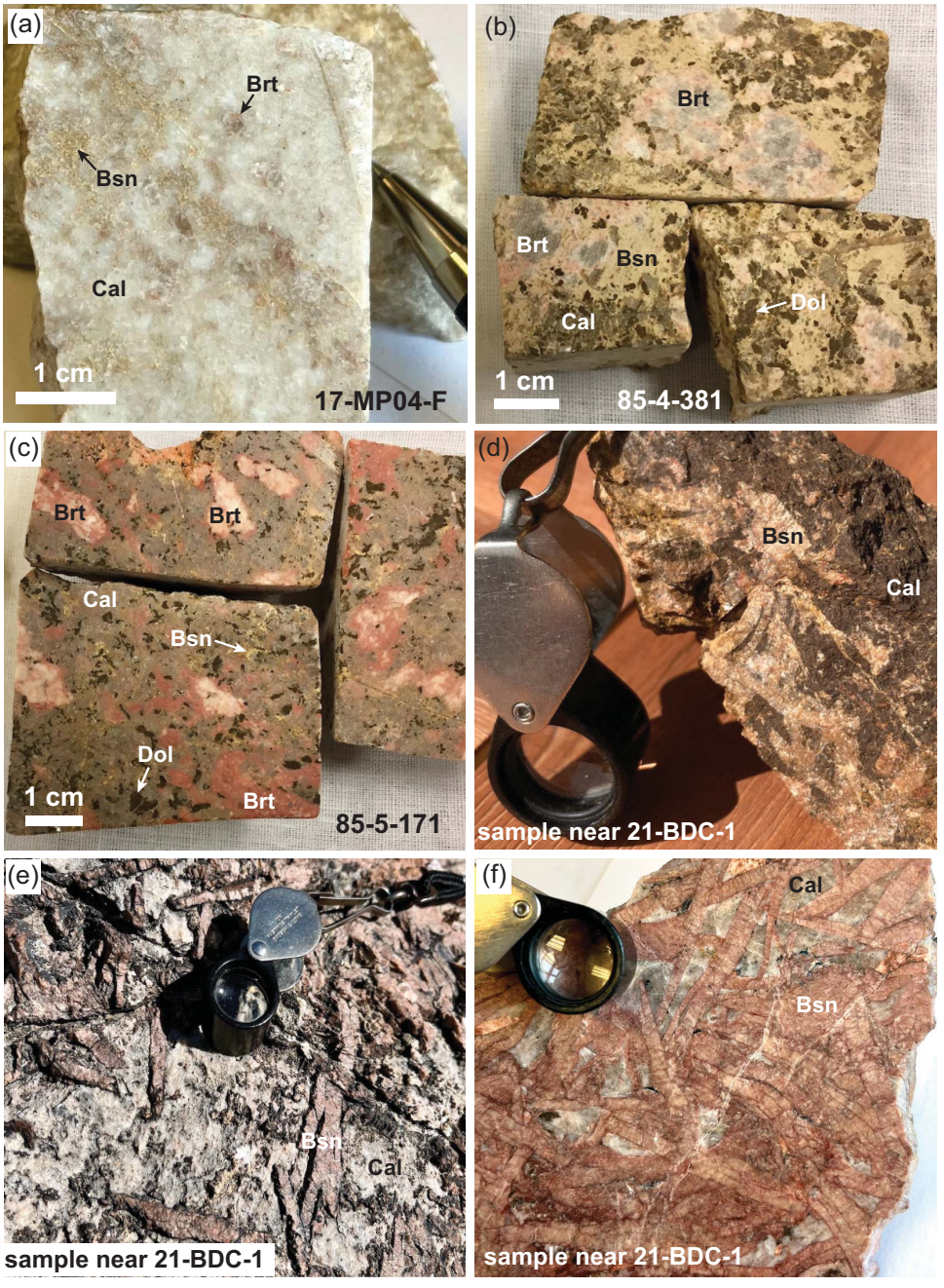

Figure 2. Hand sample photos showing the textures and mineralogy within Mountain Pass carbonatite stock and dike samples (photos by Kathryn Watts, USGS, 2021–2025). **(a)** Dump sample from the stock showing a predominantly white calcite matrix, scattered gray and pink baryte phenocrysts, and tan interstitial bastnasite. **(b)** Drill core sample from the stock showing gray and white baryte phenocrysts with pink margins set in a matrix of gray-tan calcite, dark brown dolomite, and massive tan-yellow bastnasite. **(c)** Drill core sample from the stock showing white and pink baryte phenocrysts set in a matrix of tan calcite, dark brown dolomite, and tan-yellow interstitial bastnasite. **(d)** Carbonatite dike sample showing tan-pink bastnasite crystals in a brown calcitic (and silicified) matrix. Hand lens (2 cm wide loupe) for scale. **(e)** Carbonatite dike sample showing pink bastnasite crystals that are in positive relief from the gray calcitic groundmass. **(f)** Carbonatite dike sample showing extremely coarse pink bastnasite crystals with patches of gray and white calcitic matrix. Mineral abbreviations: Brt = baryte; Cal = calcite; Dol = dolomite; Bsn = bastnäsite.

phenocrysts and matrix material, including earlier formed, interstitial bastnäsite crystals (e.g., sahamalite veins crosscutting matrix bastnäsite in Fig. 6e). Veins of calcite crosscut bastnäsite crystals in the groundmass and sometimes contain fine-grained bastnäsite (Fig. 6f). Small bastnäsite crystals surround and are intergrown with celestine replacement rims on baryte phenocrysts (Fig. 6d) and bastnäsite crystals are commonly crosscut by celestine veins (Fig. 6g). Although some lenses of carbonatite in the composite stock have relatively coarse (≥ ~1 mm length) bastnäsite crystals (e.g., Figs. 6a, 6f, and 6g), these textures are

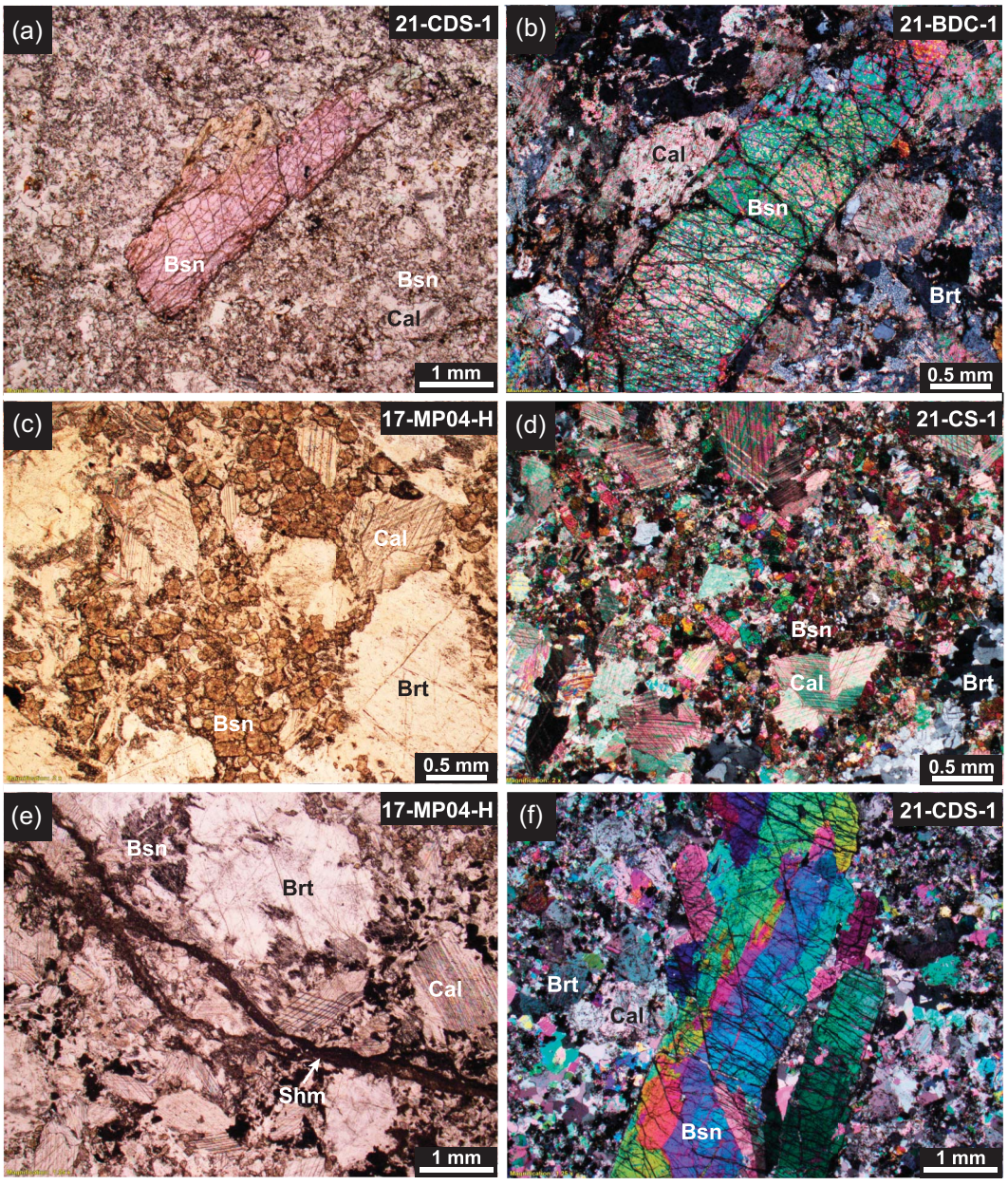

Figure 3. Thin section photomicrographs showing bastnäsite and other minerals within Mountain Pass carbonatite samples. (**a**) Plane-polarized light (PPL) image of a large, pleochroic (pink-tan) bastnäsite phenocryst in a matrix of intergrown bastnäsite and calcite. (**b**) Cross-polarized light (CPL) image of large bastnäsite crystals with high-order interference colors. (**c**) PPL image of carbonatite ore sample with small bastnäsite grains (brown) interstitial to and surrounding calcite and baryte crystals. (**d**) CPL image of carbonatite ore sample with small bastnäsite grains (brighter interference colors) interstitial to and surrounding calcite and baryte crystals. (**e**) PPL image of sahamalite vein (dark brown) crosscutting calcite, baryte, and matrix material. (**f**) CPL image of large bastnäsite crystal with patchy, irregular zoning. Small bastnäsite crystals are intergrown with calcite and baryte in the groundmass. Mineral abbreviations: Brt = baryte; Bsn = bastnäsite; Cal = calcite; Shm = sahamalite.

uncommon in the samples we have examined. This is one of the main textural differences from the dikes, for which coarse bastnäsite crystallization is nearly ubiquitous (e.g., Figs. 2d, 2e, 2f, 3a, 3b, 3f, and 6b). Breccias within the stock are present at all scales, from tens of meters to millimeters, and fine-grained bastnäsite forms a thin matrix between breccia clasts (e.g., Fig. 6h).

REE Carbonate Mineral Chemistry

The chemistry of Mountain Pass REE carbonate minerals was investigated with >500 in situ EPMA analyses (Table 4; Online Materials[1] Appendix B) (Watts and Andersen 2025). Fluorcarbonate minerals are Ce-dominant with REE concentrations as follows: Ce > La > Nd > Pr > Sm > Eu and lower (often below detection limit) concentrations of Gd, Y, and Th (Table 4).

Table 1. EPMA acquisition parameters

Elements	Oxides	X-ray lines	Spectrometer crystal	On-peak count times (s)	Mean detection limits (oxide percent)	Standard
Mg	MgO	*K*α	TAP	80	0.014	Forsterite
Ca	CaO	*K*α	PETL	60	0.017	Calcite
Mn	MnO	*K*α	LiFL	20	0.067	Spessartine
Fe	FeO	*K*α	LiFL	20	0.087	Synthetic fayalite
Sr	SrO	*L*α	PETL	40	0.046	Celestine
Y	Y_2O_3	*L*α	PETL	60	0.040	YPO_4
La	La_2O_3	*L*α	LiF	70	0.245	$LaPO_4$
Ce	Ce_2O_3	*L*α	LiF	70	0.235	$CePO_4$
Pr	Pr_2O_3	*L*α	LiF	70	0.231	$PrPO_4$
Nd	Nd_2O_3	*L*α	LiF	70	0.246	$NdPO_4$
Sm	Sm_2O_3	*L*α	LiFL	100	0.073	$SmPO_4$
Eu	Eu_2O_3	*L*α	LiFL	100	0.080	$EuPO_4$
Gd	Gd_2O_3	*L*α	LiFL	100	0.093	$GdPO_4$
Th	ThO_2	*M*α	PETL	40	0.057	ThO_2
F	F	*K*α	TAP	80	0.036	CaF_2

Bastnäsite is the main REE mineral in both the dikes and the stock, with parisite second in abundance. Ca-bearing REE carbonates such as parisite are present in both the dikes and the stock, though in the studied samples, they are more abundant in dikes as rims on bastnäsite phenocrysts (Fig. 7). Four minerals and at least two intermediate compositional domains of the bastnäsite–synchysite series have been identified: bastnäsite, B_2S, B_3S_2, parisite, röntgenite (or possibly B_3S_4), and synchysite (Fig. 8a). Intermediate compositions (e.g., polysomes B_2S and B_3S_2; Table 2) are known to arise from the modularity of stacked sequences and are typically observed at the nanometer or atomic scale through transmission electron microscopy (TEM) studies (cf. Van Landuyt and Amelinckx 1975; Wu et al. 1998; Meng et al. 2001a, 2001b; Ciobanu et al. 2022). Intermediate compositions of the bastnäsite–synchysite series may also result from sub-microscopic compositional faults, matching only by coincidence the composition of a polysome (Conconi et al. 2023). In Mountain Pass samples, the more uncommon compositions (B_2S, B_3S_2, röntgenite) on apparently homogenous lamellae at the tens of micrometers scale can be distinguished by both EPMA chemistry and BSE intensity (Figs. 7 and 8a). These methods alone cannot confirm whether the domains are truly ordered or result from compositional faults (polysomatic faults). Sahamalite was found in a cross-cutting veinlet of a single sample of the stock (Figs. 3e and 6e).

Atomic proportions in atoms per formula unit (apfu) of F^- (and OH^- calculated by difference from F^-), in Mountain Pass bastnäsite vary widely from end-member bastnäsite [$REE(CO_3)F$] to hydroxylbastnäsite [$REE(CO_3)(OH)$] (Fig. 8b). Only one sample (85-5-171) was found to contain end-member hydroxylbastnäsite with about 0.02 apfu F^- and 0.98 apfu OH^-. Most dike samples contain bastnäsite with 1.0 to 1.2 apfu F^- and 0 apfu OH^- (Fig. 8b). Two populations of partially hydroxylated bastnäsite with about 0.8 to 0.3 apfu F^- are present, one with high Nd/La apfu values >0.4 ("Group 1" samples 85-9-9 and 85-9-59) and the other with <0.4 Nd/La ("Group 2" samples 17-MP-4H-1 and 84-6-125) (Fig. 8b). Our sample set appears to show incomplete solid solution between $REE(CO_3)F$ and $REE(CO_3)(OH)$. Bastnäsite is a hexagonal mineral in the space group $P\bar{6}2c$, which Yang et al. (2008) show is capable of accommodating OH^-, but the extent of OH^- substitution without causing a transformation from $P\bar{6}2c$ to the $P\bar{6}$ structure of hydroxylbastnäsite is unknown. The observed compositional gap in our bastnäsite-hydroxylbastnäsite data from 0.3 to 0.1 apfu F^- (Fig. 8b) could indicate a limit of about 70% OH^- in the F-site; however, if the analyses classified as partially hydroxylated bastnäsite possess $P\bar{6}$ symmetry, then the limit of OH^- in the $P\bar{6}2c$ structure is probably closer to 20% (i.e., apfu F^- of 0.8).

Representative samples were analyzed by Raman spectroscopy to confirm qualitatively that the proportion of OH^- increases from bastnäsite to partially hydroxylated bastnäsite to hydroxylbastnäsite (Fig. 9). Twelve spectra are organized relative to their OH^- proportions and visually prominent bands in the OH^- stretching region of 3200–3650 cm^{-1} (Fig. 9a–9b). Those classified as bastnäsite and partially hydroxylated bastnäsite also display a single prominent band at 1092–1094 and 1086–1091 cm^{-1}, respectively (Fig. 9c). A single prominent band at ~1095 cm^{-1} for near end-member bastnäsite is consistent with results reported by Conconi et al. (2023) and Frost and Dickfos (2007). In parisite, synchysite, and intermediate polysomes, the $\nu_1(CO_3)^{2-}$ symmetric stretching around 1095 cm^{-1} is split into two or three bands (Frost and Dickfos 2007; Conconi et al. 2023). For hydroxylbastnäsite, Yang et al. (2008) report three prominent bands at 1080, 1087, and 1098 cm^{-1} in the CO_3^{2-} symmetrical stretching region, but in our samples of Mountain Pass hydroxylbastnäsite there are two prominent bands at 1074–1075 and 1090–1092 cm^{-1} (Fig. 9c). The intense Raman band at 965 cm^{-1} for hydroxylbastnäsite reported by Frost and Dickfos (2007) was not observed in the Mountain Pass samples. In the OH^- stretching region, three to five bands are commonly identified in the range 3200–3650 cm^{-1} for partially hydroxylated bastnäsite and hydroxylbastnäsite (Figs. 9a–9b), consistent with the spectra reported by Frost and Dickfos (2007). Hydroxylbastnäsite spectra display the most prominent bands (3488, 3627, 3644 cm^{-1}), which are shifted to higher wave numbers (Fig. 9b). The most notable changes of spectral features (hydroxylbastnäsite sample 85-5-171) are consistent with the observed compositional gap in apfu F^- (Fig. 8b). They may correspond with the structural transformation from $P\bar{6}2c$ to $P\bar{6}$ symmetry.

High LREE relative to HREE in carbonate ore minerals is the main contributor to the characteristic steep LREE-enriched chondrite-normalized REE patterns for Mountain Pass carbonatites (e.g., Fig. 5b). Though only the LREE are enriched to such high concentrations, the carbonate ore minerals also contain moderate concentrations of Sm, Eu, Gd, and Y (Table 4), which progressively increase from bastnäsite to parisite to synchysite, as shown by chondrite- and carbonatite-normalized REE patterns (Figs. 8c–8d) and ratios of summed Sm+Eu+Gd+Y to total REEs (TREE) (Fig. 8e). Like observed for other carbonatite-hosted fluorcarbonate resources (e.g., Bear Lodge, U.S.A.; Khibina, Russia; Tamazert, Morocco), the proportion of HREE is typically greater in the more Ca-rich fluorcarbonate varieties (Wall 2000; Andersen, et al. 2017, 2019). In this study, bastnäsite is observed to have the lowest Sm+Eu+Gd+Y/TREE value, with values for B_2S, B_3S_2, parisite, röntgenite, and synchysite increasing in relative order (Fig. 8e).

Table 2. Compilation of Ca-REE fluorcarbonate minerals and intermediate mixed-layer structures

Ca-REE fluorcarbonate minerals and intermediate mixed-layer structures		Formula	General formula	Alternative formula (fluocerite and vaterite components)	Bastnäsite-synchysite layers	Ca:REE ratio	Ca/(Ca+REE) ×100	Reference(s) in Online Materials[1] Appendix A
Bastnäsite subgroup	Bastnäsite-(Ce)	$Ce(CO_3)F$	$REE(CO_3)F$	$(REEF)\cdot(CO_3)$	B	0.000	0.00	1, 19, 31, 33, 34, 36
	Bastnäsite-(La)	$La(CO_3)F$						4
	Bastnäsite-(Y)	$Y(CO_3)F$						5
Bastnäsite subgroup (hydroxylbastnasite series)	Hydroxylbastnäsite-(Ce)	$Ce(CO_3)(OH)$	$REE(CO_3)(OH)$	$(REEOH)\cdot(CO_3)$	B	0.000	0.00	6, 24, 25
	Hydroxylbastnäsite-(La)	$La(CO_3)(OH)$						7, 30
	Hydroxylbastnäsite-(Nd)	$Nd(CO_3)(OH)$						7, 8
	B_5S_2	$Ca_2Ce_7(CO_3)_9F_7$	$REE_7Ca_2(CO_3)_9F_7$	$7(REEF)\cdot7(CO_3)\cdot2[Ca(CO_3)]$	B_5S_2	0.286	22.22	38
	B_2S	$CaCe_3(CO_3)_4F_3$	$REE_3Ca(CO_3)_4F_3$	$3(REEF)\cdot3(CO_3)\cdot[Ca(CO_3)]$	B_2S	0.333	25.00	15, 16, 17, 18, 20, 33, 34, 36
	$B_{18}S_{10}$	$Ca_{10}Ce_{28}(CO_3)_{38}F_{28}$	$REE_{28}Ca_{10}(CO_3)_{38}F_{28}$	$28(REEF)\cdot28(CO_3)\cdot10[Ca(CO_3)]$	$B_{18}S_{10}$	0.357	26.32	38
	B_7S_4	$Ca_4Ce_{11}(CO_3)_{15}F_{11}$	$REE_{11}Ca_4(CO_3)_{15}F_{11}$	$11(REEF)\cdot11(CO_3)\cdot4[Ca(CO_3)]$	B_7S_4	0.364	26.67	14
	$B_{10}S_6$	$Ca_6Ce_{16}(CO_3)_{22}F_{16}$	$REE_{16}Ca_6(CO_3)_{22}F_{16}$	$16(REEF)\cdot16(CO_3)\cdot6[Ca(CO_3)]$	$B_{10}S_6$	0.375	27.27	14
	B_3S_2	$Ca_2Ce_5(CO_3)_7F_5$	$REE_5Ca_2(CO_3)_7F_5$	$5(REEF)\cdot5(CO_3)\cdot2[Ca(CO_3)]$	B_3S_2	0.400	28.57	3, 20
	B_8S_6	$Ca_6Ce_{14}(CO_3)_{20}F_{14}$	$REE_{14}Ca_6(CO_3)_{20}F_{14}$	$14(REEF)\cdot14(CO_3)\cdot6[Ca(CO_3)]$	B_8S_6	0.429	30.00	14
	B_5S_4	$Ca_4Ce_9(CO_3)_{13}F_9$	$REE_9Ca_4(CO_3)_{13}F_9$	$9(REEF)\cdot9(CO_3)\cdot4[Ca(CO_3)]$	B_5S_4	0.444	30.77	38
Parisite subgroup	Parisite-(Ce)	$Ca(Ce,La)_2(CO_3)_3F_2$	$REE_2Ca(CO_3)_3F_2$	$2(REEF)\cdot2(CO_3)\cdot[Ca(CO_3)]$	BS	0.500	33.00	1, 3, 19, 20, 26, 27, 31, 33, 34, 36
	Parisite-(La)	$Ca(La,Nd,Ce)_2(CO_3)_3F_2$						37
	Parisite-(Nd)	$Ca(Nd,Ce,La)_2(CO_3)_3F_2$						9
	B_3S_4	$Ca_4Ce_7(CO_3)_{11}F_7$	$REE_7Ca_4(CO_3)_{11}F_7$	$7(REEF)\cdot7(CO3)\cdot4[Ca(CO3)]$	B_3S_4	0.571	36.36	3, 20
	Röntgenite-(Ce)	$Ca_2(Ce,La)_3(CO_3)_5F_3$	$REE_3Ca_2(CO3)_5F_3$	$3(REEF)\cdot3(CO_3)\cdot2[Ca(CO_3)]$	BS_2	0.667	40.00	1, 2, 3, 19, 20, 36
	BS_4	$Ca_4Ce_5(CO_3)_9F_5$	$REE_5Ca_4(CO_3)_9F_5$	$5(REEF)\cdot5(CO_3)\cdot4[Ca(CO_3)]$	BS_4	0.800	44.44	3
Synchysite subgroup	Synchysite-(Ce)	$CaCe(CO_3)_2F$	$REECa(CO_3)_2F$	$(REEF)\cdot(CO_3)\cdot[Ca(CO_3)]$	S	1.000	50.00	1, 3, 12, 19, 35, 36
	Synchysite-(Y)	$CaY(CO_3)_2F$						10, 11, 21, 29
	Synchysite-(Nd)	$CaNd(CO_3)_2F$						13, 28
Thorbastnäsite[a]		$Th(Ca,Ce)(CO_3)_2F_2\cdot3(H_2O)$	$Th(Ca,REE)(CO_3)_2F_2\cdot3(H_2O)$	NA	NA	NA	NA	32
Sahamalite[b]		$(Mg,Fe)Ce_2(CO_3)_4$	$(Mg,Fe)REE_2(CO_3)_4$	NA	NA	NA	NA	22, 23

Notes: This table was compiled from many references and may be incomplete, as numerous B*m*S*n*-type mixed-layer compounds, polysomes, and polytypes have been observed. The complexity of Ca-REE fluorcarbonates arises from microsyntaxy and polytypic modularity through variations in the stacking arrangements of REEF, CO_3, and Ca-bearing layers. Other intermediate compositions (e.g., B_6S, B_5S, B_4S, and B_3S) are possible as a result of polysomatic faults within parisite (Capitani 2019).

[a] Little is known about the structure of thorbastnäsite or how it relates to the bastnäsite-synchysite group.

[b] Sahamalite is a REE-bearing anhydrous compound carbonate mineral containing Mg and Fe—it does not belong to the hydroxyl- or halogen-bearing groups listed above. For recent studies of the bastnäsite-synchysite group, readers are directed to Ciobanu et al. (2017, 2022), Capitani (2019, 2020), and Conconi et al. (2023).

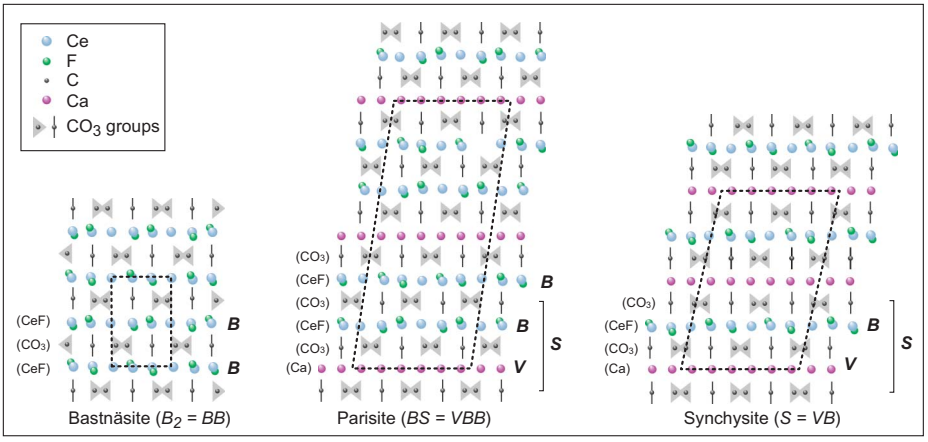

Figure 4. Lattice structures for REE fluorcarbonate ore minerals showing the different building layers stacked along the vertical c-axis, composed as stacks of cell components B (bastnäsite; $CeCO_3F$), V (vaterite; $CaCO_3$), and S (synchysite; $CeCaCO_3F$) [modified from Capitani (2020) and Conconi et al. (2023)]. The unit cell is shown as a dashed black line. Refer to Table 2 for chemical formulas of REE carbonate minerals and intermediate mixed-layer structures relevant to this study.

Table 3. Carbonatite whole-rock geochemical data

Sample number	Description	Carbonatite type by chemistry (this study)	Carbonatite type as mapped (Castor 2008)	Latitude (°N)	Longitude (°W)	CO_2 wt%	CaO wt%
84-6-125	Sulphide Queen carbonatite stock	Calcite-dolomite	Dolomite	35.47794	−115.53140	20.9	16.4
84-6-134	Sulphide Queen carbonatite stock	Calcite-dolomite	Dolomite	35.47794	−115.53140	30.9	21.2
84-6-138	Sulphide Queen carbonatite stock	Calcite-dolomite	Dolomite	35.47794	−115.53140	18.7	15.2
85-1-162	Sulphide Queen carbonatite stock	Calcite	Calcite	35.47739	−115.53175	12.6	15.7
85-1-228	Sulphide Queen carbonatite stock	Calcite	Calcite	35.47739	−115.53175	27.6	34.7
85-1-306	Sulphide Queen carbonatite stock	Calcite-dolomite	Calcite-dolomite	35.47739	−115.53175	27.1	16.6
85-1-324	Sulphide Queen carbonatite stock	Calcite-dolomite	Dolomite	35.47739	−115.53175	19.3	12.9
85-1-448	Sulphide Queen carbonatite stock	Calcite-dolomite	Calcite-dolomite	35.47739	−115.53175	9.9	6.4
85-1-611	Sulphide Queen carbonatite stock	Calcite	Calcite	35.47739	−115.53175	17.5	22.1
85-4-381	Sulphide Queen carbonatite stock	Calcite-dolomite	Dolomite	35.47832	−115.53213	11.2	7.5
85-4-490	Sulphide Queen carbonatite stock	Calcite	Calcite	35.47832	−115.53213	19.4	24.1
85-5-171	Sulphide Queen carbonatite stock	Calcite	Calcite-dolomite	35.47845	−115.53153	16.5	16.5
85-9-9	Sulphide Queen carbonatite stock	Calcite	Calcite	35.47953	−115.53182	17.9	22.0
85-9-59	Sulphide Queen carbonatite stock	Calcite	Calcite	35.47953	−115.53182	20.3	25.0
85-9-67	Sulphide Queen carbonatite stock	Calcite	Calcite	35.47953	−115.53182	19.2	23.4
85-12-304	Sulphide Queen carbonatite stock	Calcite	Breccia	35.47704	−115.53105	27.0	26.8
85-12-317	Sulphide Queen carbonatite stock	Calcite	Breccia	35.47704	−115.53105	28.4	35.8
17MP04A	Sulphide Queen carbonatite stock	Calcite	NA	35.48292	−115.53236	12.4	13.4
17MP04B	Sulphide Queen carbonatite stock	Calcite-dolomite	NA	35.48292	−115.53236	24.1	15.3
17MP04C	Sulphide Queen carbonatite stock	Calcite-dolomite	NA	35.48292	−115.53236	27.1	18.4
17MP04D	Sulphide Queen carbonatite stock	Calcite	NA	35.48292	−115.53236	22	24.1
17MP04E	Sulphide Queen carbonatite stock	Calcite-dolomite	NA	35.48292	−115.53236	29.6	18.3
17MP04F	Sulphide Queen carbonatite stock	Calcite-dolomite	NA	35.48292	−115.53236	30.3	18.9
17MP04G	Sulphide Queen carbonatite stock	Calcite-dolomite	NA	35.48292	−115.53236	30.8	18.8
17MP04H	Sulphide Queen carbonatite stock	Calcite	NA	35.48292	−115.53236	10.1	10.3
17MP04I	Sulphide Queen carbonatite stock	Calcite	NA	35.48292	−115.53236	6.93	6.23
21-CS-1	Sulphide Queen carbonatite stock	Calcite	NA	35.46956	−115.52874	14.8	16.9
21-CDS-1	Carbonatite dike	Calcite	NA	35.46177	−115.51235	36.1	43.3
18-MP-02	Carbonatite dike	Calcite-dolomite	NA	35.48869	−115.53547	26.5	14.8
21-BDC-1	Carbonatite dike	Calcite	NA	35.48906	−115.53716	27.2	29.6

MgO wt%	Fe_2O_3 wt%	S wt%	BaO wt%	SrO wt%	F wt%	MnO wt%	Na_2O wt%	P_2O_5 wt%	SiO_2 wt%	TiO_2 wt%	Al_2O_3 wt%	H_2O wt%
5.75	1.91	4.79	19.4	2.0	0.70	0.31	0.35	0.72	<0.01	0.06	0.04	0.71
10.40	3.37	2.42	10.1	2.2	0.47	0.51	0.05	0.34	0.2	0.08	<0.01	0.65
3.83	1.00	3.28	11.3	2.8	1.56	0.19	0.33	0.08	0.01	0.04	0.02	0.91
0.30	3.77	5.64	28.3	2.3	0.04	0.14	0.41	3.49	2.71	0.11	0.28	0.31
0.20	0.23	3.71	17.0	3.0	0.14	0.36	0.2	0.11	3.09	0.05	0.03	0.31
9.30	2.21	3.29	9.0	3.6	1.01	0.57	0.06	0.45	<0.01	0.03	<0.01	0.52
7.21	1.75	5.28	18.7	6.7	0.46	0.47	0.33	0.13	0.3	0.06	0.03	0.47
3.46	0.91	2.03	28.7	8.7	0.57	0.19	0.45	0.28	0.27	0.09	0.05	0.57
0.04	0.18	6.12	12.4	14.1	0.74	0.14	0.22	0.04	<0.01	0.04	0.02	0.32
2.19	0.53	4.33	26.6	6.9	1.36	0.09	0.46	0.2	0.11	0.08	0.05	0.68
0.05	0.08	5.98	8.1	12.9	0.62	0.18	0.19	0.04	0.28	0.03	0.02	0.68
0.11	0.35	4.37	20.3	0.9	0.17	0.1	0.38	0.48	7.1	0.07	0.02	1.07
1.64	2.25	1.21	5.2	0.7	0.59	0.42	0.14	0.62	26.7	0.02	<0.01	1.13
0.43	0.20	5.67	18.1	10.2	0.20	0.54	0.25	0.24	0.62	0.05	0.04	0.43
2.20	1.14	5.73	13.3	9.5	0.32	0.48	0.3	0.1	4.57	0.04	0.05	0.71
7.27	3.08	3.64	19.9	1.4	0.12	0.5	0.26	1.44	0.15	0.08	0.03	0.48
0.76	0.58	3.30	16.0	0.7	0.16	0.26	0.21	1.2	0.54	0.07	0.10	0.36
0.84	0.34	7.56	21.4	8.53	0.66	<0.01	<0.01	0.19	0.31	<0.01	0.03	0.6
9.24	1.99	3.94	13.9	4.17	0.58	0.49	<0.01	0.07	0.13	<0.01	0.01	0.4
8.84	3.61	3.97	7.24	6.17	0.52	0.55	<0.01	1.2	<0.01	<0.01	0.04	0.3
2.49	0.71	6.85	21.9	7.65	0.13	0.33	<0.01	0.17	0.06	<0.01	<0.01	0.3

Table 3. (*Continued*)

MgO wt%	Fe_2O_3 wt%	S wt%	BaO wt%	SrO wt%	F wt%	MnO wt%	Na_2O wt%	P_2O_5 wt%	SiO_2 wt%	TiO_2 wt%	Al_2O_3 wt%	H_2O wt%
11.10	2.94	3.24	13.3	3.76	0.2	0.73	<0.01	0.07	0.46	<0.01	0.01	0.4
11.30	3.04	3.87	14	3.68	0.13	0.79	<0.01	0.04	0.28	<0.01	0.02	0.3
11.70	3.34	2.97	12	3.06	0.3	0.77	<0.01	0.13	<0.01	<0.01	<0.01	0.3
0.66	0.22	7.86	26.1	7.26	0.79	<0.01	<0.01	0.15	<0.01	<0.01	0.01	0.6
0.99	3.26	3.78	17.3	0.63	0.33	0.78	<0.01	0.14	42.1	<0.01	0.06	1.1
0.05	0.17	6.95	28.9	1.37	1.31	0.09	0.12	0.08	<0.01	<0.01	0.03	0.4
0.24	1.61	0.856	3.74	0.13	0.82	0.42	0.06	0.14	0.55	<0.01	0.08	0.4
8.86	3.76	1.59	7.17	6.44	0.88	0.41	0.03	0.09	14	<0.01	0.3	0.7
0.11	0.31	0.849	3.89	0.21	2.08	0.58	0.02	0.04	2.72	<0.01	0.29	0.4

La ppm	Ce ppm	Pr ppm	Nd ppm	Sm ppm	Eu ppm	Gd ppm	Tb ppm	Dy ppm	Ho ppm	Er ppm	Tm ppm	Yb ppm	Lu ppm
39900	52700	3720	10000	634	98.5	206	11.8	31.7	3.33	8.59	0.45	2.45	0.27
30100	43000	3080	8410	552	82.5	177	10.9	29.8	3.53	7.84	0.82	3.11	0.39
76200	108000	7970	21200	1310	188	393	21.4	53.9	5.36	15.2	0.91	4.7	0.56
29500	45300	3530	10300	783	127	283	19.5	51.8	6.19	15.2	1.28	7.15	0.83
5860	8706	742	2230	194	33.4	86.4	7.34	29.9	4.68	11.9	1.17	8.37	1.12
48400	77700	4200	17500	1120	116	352	19.2	37.3	4.25	9.36	0.53	2.86	0.43
28400	43300	3200	8890	559	83.3	170	8.69	22.5	2.2	5.82	0.29	1.79	0.13
33800	48600	3580	9850	647	103	224	13.2	39.1	4.61	10.4	0.73	3.59	0.24
34700	53400	2570	11700	584	97.9	353	20.7	45.3	5.7	12.7	1.09	6.1	0.87
52100	70400	5080	13400	768	113	243	12.7	25.5	2.69	7.32	0.35	1.77	0.26
42400	62900	4920	14900	1180	150	436	25.7	57.2	6.86	15	1.5	6.9	1.07
54900	79200	5960	16300	997	147	300	15.5	38.5	3.51	9.6	0.55	2.58	0.37
29900	49900	4130	12200	848	131	272	15.7	42.4	4.21	10	0.55	2.65	0.24
9870	18600	1640	5030	407	69.8	151	10.1	35.1	4.66	10.4	0.96	2.89	0.33
16200	28900	2450	7580	600	99.4	212	13.2	41.4	4.59	10.5	0.7	4.26	0.39
1240	2338	236	812	106	24.8	63.1	6.34	31.5	3.96	9.09	0.73	4.5	0.39
11400	19500	1600	4990	453	82.1	191	14.2	47.9	6.43	12.8	1.56	7.84	1.08
48600	64400	5330	15800	910	140	205	16.7	38.7	4.7	7.77	–	2.95	0.37
40000	53700	4610	13800	788	122	198	16.6	34.5	3.95	6.6	–	2.33	0.27
40400	54000	4390	12500	729	114	216	17.4	39	4.97	8.84	–	3.41	0.34
7320	9670	876	2550	169	28.2	53.4	4.77	13.9	2.04	4.47	–	3.47	0.58
24100	31200	2900	8600	500	72.2	112	8.86	23.6	2.98	5.15	–	2.31	0.34
17800	24400	2120	6500	389	57.8	107	8.59	20.7	2.55	4.61	–	2.18	0.32
24100	33100	2990	8800	538	81.2	143	12.4	26.6	3.17	5.86	–	2.41	0.36
55500	71800	6190	18000	1050	153	263	21.1	43.1	5.12	8.63	–	2.36	0.28
23500	33100	3030	9200	545	83.4	145	12.1	32.5	4.65	10.5	–	7.25	1.02
34900	52100	4560	12100	724	114	303	22.8	32.7	3.78	5.22	0.53	2.76	0.32
13800	26600	2970	10300	1540	347	882	74.2	187	20.7	32.3	2.7	14.9	1.56
16600	33000	3800	13500	1780	424	1120	113	355	46.8	81.6	8.11	36.5	4.23
55200	84900	8000	24500	2040	328	950	56.1	149	19.5	34.4	3.57	20.6	2.56

Th ppm	U ppm	Y ppm	Pb ppm	As ppm	Co ppm	Cu ppm	Ge ppm	Nb ppm	Sb ppm	Ta ppm	Zr ppm
150	10.2	93.3	74	194	7.4	92	84	8.5	22.3	0.8	1.8
114	24.2	79.5	62	227	6	544	62	52.9	33.7	0.8	5
393	171	151	159	468	6.5	149	159	7.9	109	1	1.3
2780	37.9	167	3390	190	6.1	127	77	174	0.7	1.8	2.6
154	4	132	111	39	2.2	10	17	10.4	4.8	0.8	8.5
233	19.1	110	480	287	9	13	104	1.9	31.7	0.8	<0.5
157	19.1	54.5	123	178	5	15	66	<0.1	10.1	1.4	<0.5
142	11.9	108	49	201	2.9	10	80	57.6	4.3	1.5	1.6
170	1.4	150	23	169	2.5	8	65	0.3	0.1	1	<0.5
172	59	73.1	170	279	1.8	10	103	0.5	23.5	1.1	0.7
366	2.29	181	47	246	1.2	11	96	0.6	1.2	0.9	<0.5
297	10.3	84.3	312	318	1	10	121	15.1	9	0.8	0.8
297	4.92	110	4700	263	6.8	20	96	10.2	5.6	0.9	2.3
83.4	1.3	129	1170	94	0.5	9	37	<0.1	<0.1	0.7	<0.5
140	2.37	134	1780	150	3.2	9	65	0.8	<0.1	0.9	0.6
48.1	56.8	90.2	260	44	6.4	110	6	298	3.3	3.9	6.5
418	16.2	153	254	122	1.7	58	36	88.1	1.8	1.4	3.3
348	1.97	105	57	2230	1.5	7	45	2.9	15.7	<0.5	0.9
255	6	80.7	91	1720	4.3	17	40	0.8	2.4	<0.5	<0.5
268	51.9	103	105	1790	20.8	35	36	57.7	14.2	<0.5	4.8
37.5	3.28	48.2	46	334	1.3	6	7	8	2.2	<0.5	<0.5
173	1.88	59.5	185	986	7	27	24	0.7	1.8	<0.5	<0.5
115	2.01	51.3	296	768	7	27	18	0.5	1.4	<0.5	<0.5
177	2.62	61.3	237	1060	7.5	32	25	1	1.7	<0.5	<0.5
337	3.14	93.9	79	2280	1.2	6	50	0.9	0.6	<0.5	<0.5
190	51.5	99.9	3370	1340	8.7	7	27	3.4	15.7	<0.5	0.7
243	14.4	88.6	287	394	<0.5	<5	3	0.9	0.6	<0.5	0.8
94.6	9.01	582	1940	409	1.2	<5	23	3.1	<0.1	<0.5	2.0
536	57.4	1070	118	423	27.3	<5	28	3.8	0.7	<0.5	8.0
533	28.7	470	538	763	<0.5	<5	53	41	<0.1	<0.5	39.5

Note:– indicates no data.

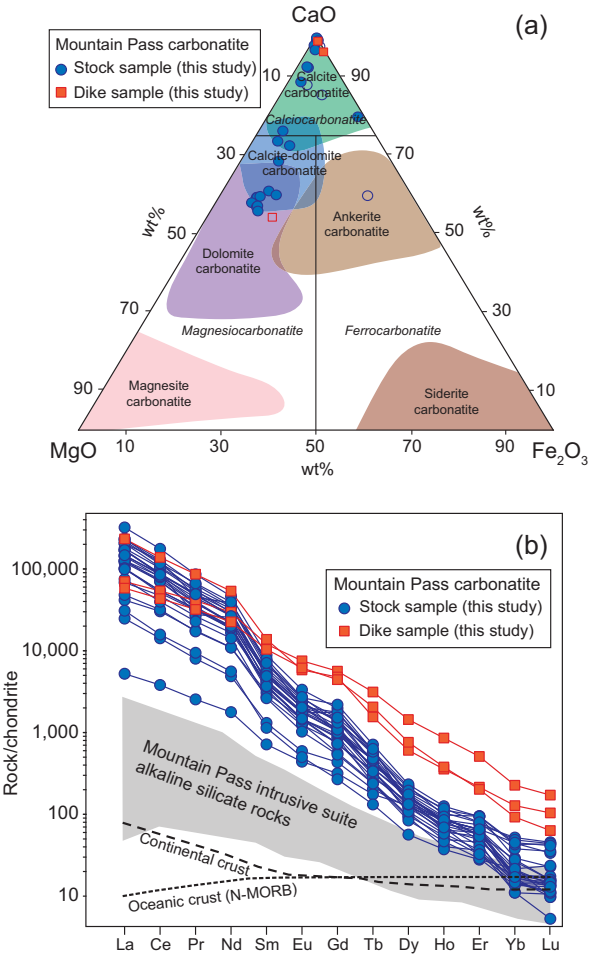

Figure 5. Whole-rock geochemical data for Mountain Pass carbonatite samples. (**a**) Carbonatite ternary classification diagram. Classification fields from Le Maitre et al. (1989) and natural plutonic carbonatite samples (transparent colored polygons) from Kamenetsky et al. (2021). Open symbols show samples with >5 wt% SiO_2. (**b**) Mountain Pass carbonatite REE data shown on a chondrite-normalized plot. The gray shaded field shows the chondrite-normalized REE concentrations of alkaline silicate rocks of the Mountain Pass intrusive suite, from Watts et al. (2024). Chondrite values are from McDonough and Sun (1995). Average crustal values are shown in the black dashed lines. Present Earth continental crust is from Taylor and McLennan (1981) and oceanic crust (N-MORB; normal mid-ocean ridge basalt) is from Sun and McDonough (1989).

Discussion

Complexity of REE Carbonate Ore Mineralogy at Mountain Pass

Mountain Pass has long been upheld as an archetypal example of a primary magmatic carbonatite deposit (e.g., Mariano 1989; Castor 2008; Verplanck et al. 2016), but recent high spatial resolution studies of its constituent minerals provide evidence for magmatic and metasomatic processes in its formation (e.g., Benson and Watts 2024). Our study of carbonate REE minerals confirms a complex mineralization history. REE-bearing carbonate minerals identified in this study include bastnäsite, hydroxylbastnäsite, parisite, synchysite, röntgenite, sahamalite, and at least two syntaxial domains compositionally similar to B_2S, B_3S_2 polysomes (Figs. 7 and 8). The presence, proportion, and textural contexts of these minerals vary between samples, within samples, and even within single crystals in samples (e.g., Fig. 7). Although zoning of REE carbonate minerals can sometimes be discerned optically (e.g., patches of different interference colors in a large, zoned bastnäsite crystal in Fig. 3f), usually the zoned minerals do not display optical differences and require high spatial resolution (micrometer-scale) chemical mapping to resolve. Carbonate ore minerals occur as zoned and unzoned phenocrysts, fine-grained interstitial crystals, in cross-cutting veins and veinlets, and within and lining breccia fragments, consistent with multiple stages of REE mineralization (Figs. 6 and 7).

In the carbonatite stock, fine-grained bastnäsite crystals line the margins of baryte, calcite, and dolomite phenocrysts (Fig. 6d). Bastnäsite and other REE-bearing carbonate minerals form veins that crosscut phenocrysts and matrix material, including earlier formed, interstitial bastnäsite crystals (e.g., sahamalite veins crosscutting matrix bastnäsite in Fig. 6e). Crosscutting veins of calcite are also common. Some contain small fragments of bastnäsite and other minerals and crosscut larger, euhedral bastnäsite crystals in the groundmass (Fig. 6f). The prevalence of bastnäsite and other REE carbonate minerals in interstitial and cross-cutting contexts suggests that REE mineralization in the carbonatite stock was at least in part a relatively late-stage event (i.e., after primary igneous crystallization).

In contrast to the stock, the carbonatite dikes are generally characterized by coarse bastnäsite crystals readily apparent to the naked eye (e.g., Figs. 2d, 2e, and 2f). Although some crystals appear to be mostly euhedral and unzoned, the majority exhibit a remarkable degree of chemical heterogeneity and complex zoning (e.g., Figs. 6b and 7). In general, the dikes have a larger proportion of the Ca-bearing REE carbonate minerals parisite and synchysite than the stock. Because these minerals commonly host a greater proportion of middle to heavy REE relative to total REE (Figs. 8c–8e), the whole-rock chemical data also reflect this distinguishing characteristic with higher concentrations of elements Sm-Lu (atomic numbers 62 to 71) in the dikes than observed for the carbonatite stock (Fig. 5b). The different bastnäsite contexts in the stock and dike samples may be due to the dikes representing an early, predominantly igneous phase of carbonatite formation, whereas the stock is a mixed unit that was heavily reworked chemically and physically by late-stage hydrothermal alteration and brecciation (see next discussion section).

The observed crystal zoning, from bastnäsite cores to more Ca-rich parisite and synchysite rims in the dikes, is consistent with early-forming bastnäsite preferentially incorporating the lightest REE (La, Ce), with heavier REE entering the crystal structures of Ca-REE fluorcarbonates during later stages of crystallization or recrystallization (e.g., Conconi et al. 2025). The Ca-REE fluorcarbonates can be described in terms of bastnäsite and vaterite (μ-$CaCO_3$) end-members with changes in the stacking sequences of these components giving rise to compositional variability (Fig. 4). In bastnäsite, REE are coordinated in $REEO_6F_3$ polyhedra, whereas synchysite hosts additional alkaline earth

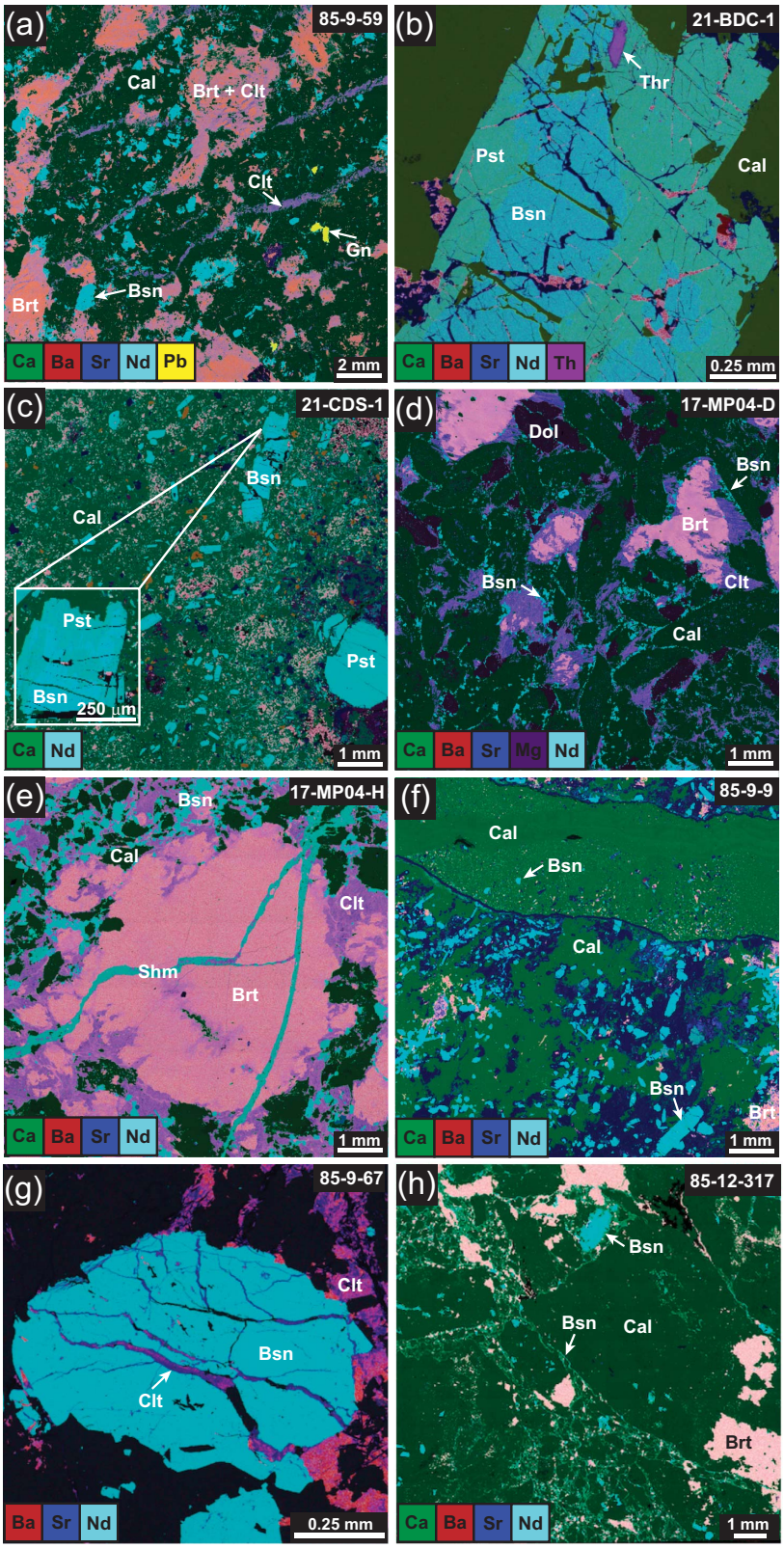

Figure 6. Layered elemental maps of carbonatite samples acquired by SEM-EDS. Boxes in the bottom-left corner of each panel show the elements and their assigned colors. (**a**) Baryte phenocrysts with celestine replacement and cross-cutting veins of celestine. Abundant bastnäsite and sparse galena are interstitial minerals in a calcitic matrix. (**b**) Large, tabular bastnäsite phenocryst rimmed by parisite with a thorite inclusion in the rim and cross-cutting veins of celestine and baryte. (**c**) Porphyritic texture defined by bastnäsite and parisite phenocrysts in a calcitic groundmass. Some crystals have relict bastnäsite cores surrounded by parisite; inset shows a magnified part of a grain in the main panel with this texture. (**d**) Baryte phenocrysts with celestine replacement rims. Fine bastnäsite crystals are interstitial and conform to the edges of calcite, dolomite, and baryte grains. (**e**) Large baryte phenocryst with celestine replacement, crosscut by a sahamalite vein. Bastnäsite crystals are intergrown with calcite in the groundmass and interstitial to baryte phenocrysts. (**f**) Bastnäsite crystals and matrix calcite are crosscut by a calcite vein that contains fine fragments of bastnäsite and baryte. (**g**) Bastnäsite crystal crosscut by celestine vein. (**h**) Microbreccia with clasts lined by fine-grained bastnäsite. Mineral abbreviations: Brt = baryte; Bsn = bastnäsite; Cal = calcite; Clt = celestine; Dol = dolomite; Gn = galena; Pst = parisite; Shm = sahamalite; Thr = thorite.

Table 4. Average REE-bearing carbonate mineral chemistry from EPMA

Mineral	B_2S	B_2S	B_3S_2	Bastnäsite	Hydroxylbastnäsite	Bastnäsite, partially hydroxylated	Bastnäsite	Parisite	Parisite	Röntgenite	Synchysite	Synchysite	Sahamalite
Sample type	Dike	Stock	Dike	Dike	Stock	Stock	Stock	Dike	Stock	Dike	Dike	Stock	Stock
N =	16	8	13	71	57	168	60	83	9	3	4	14	3
						Weight percent (wt%)							
MgO	bdl	bdl	bdl	bdl	bdl	bdl	bdl	bdl	bdl	bdl	bdl	bdl	5.96
CaO	7.30	7.35	8.34	0.07	0.05	0.04	0.16	10.19	10.37	12.28	17.41	17.55	0.08
MnO	bdl	bdl	bdl	bdl	bdl	bdl	bdl	bdl	bdl	bdl	bdl	bdl	0.30
FeO	bdl	bdl	bdl	bdl	bdl	bdl	bdl	bdl	bdl	bdl	bdl	bdl	2.12
SrO	0.17	0.15	0.20	bdl	bdl	bdl	0.09	0.14	0.04	0.08	0.04	0.08	0.08
Y_2O_3	0.19	0.28	0.19	0.07	bdl	bdl	bdl	0.28	0.44	0.43	1.10	0.51	bdl
La_2O_3	18.44	22.22	17.89	23.55	26.34	24.97	26.12	17.85	21.67	15.03	11.15	15.52	22.17
Ce_2O_3	31.00	29.30	30.80	36.11	36.61	36.49	35.98	28.91	26.88	27.96	24.06	24.20	29.85
Pr_2O_3	3.13	2.91	3.01	3.16	3.35	3.19	2.97	2.97	2.69	2.88	2.98	2.74	2.23
Nd_2O_3	10.90	9.86	10.78	10.78	10.24	9.98	9.04	10.98	9.62	10.31	11.48	10.26	6.51
Sm_2O_3	1.14	0.78	1.11	0.80	0.42	0.51	0.49	1.14	0.75	1.35	1.97	0.89	0.22
Eu_2O_3	0.28	0.20	0.28	0.24	0.17	0.16	0.15	0.32	0.24	0.31	0.55	0.29	0.10
Gd_2O_3	0.45	0.43	0.48	bdl	bdl	bdl	bdl	0.58	0.50	0.63	1.43	0.73	bdl
ThO_2	0.06	0.07	bdl	bdl	0.05	0.08	0.15	0.18	0.08	bdl	bdl	bdl	bdl
F	8.13	8.30	7.90	9.56	0.20	5.19	8.94	7.87	7.70	7.97	6.62	6.41	bdl
CO_2, calc by diff.	22.22	18.18	21.76	17.07	22.54	21.55	18.50	19.38	19.38	24.12	23.99	21.10	30.37
$-O\equiv F$	3.43	−0.02	2.77	−1.56	−0.08	−2.19	−2.59	−0.79	0.35	3.36	2.79	0.27	0.00
ΣREO	65.54	65.97	64.55	74.71	77.12	75.29	74.75	63.03	62.79	58.90	54.73	55.13	61.09
CaO/REO×100	11.14	11.14	12.93	0.09	0.06	0.05	0.21	16.17	16.52	20.85	31.81	31.84	0.14
						Atoms per formula unit (apfu)							
Mg^{2+}	bdl	bdl	bdl	bdl	bdl	bdl	bdl	bdl	bdl	bdl	bdl	bdl	0.797
Ca^{2+}	0.982	0.980	1.912	0.003	0.002	0.001	0.006	0.958	0.974	1.880	0.957	0.958	0.008
Mn^{2+}	bdl	bdl	bdl	bdl	bdl	bdl	bdl	bdl	bdl	bdl	bdl	bdl	0.023
Fe^{2+}	bdl	bdl	bdl	bdl	bdl	bdl	bdl	bdl	bdl	bdl	bdl	bdl	0.159
Sr^{2+}	0.012	0.011	0.025	bdl	bdl	bdl	0.002	0.007	0.002	0.007	0.001	0.002	0.004
Y^{3+}	0.013	0.018	0.022	0.001	bdl	bdl	bdl	0.013	0.021	0.033	0.030	0.014	bdl
La^{3+}	0.854	1.020	1.410	0.317	0.343	0.333	0.350	0.577	0.700	0.792	0.212	0.291	0.734
Ce^{3+}	1.424	1.335	2.412	0.482	0.474	0.484	0.478	0.929	0.862	1.463	0.452	0.451	0.981
Pr^{3+}	0.143	0.132	0.234	0.042	0.043	0.042	0.039	0.095	0.086	0.150	0.056	0.051	0.073
Nd^{3+}	0.488	0.438	0.823	0.140	0.129	0.129	0.117	0.344	0.301	0.526	0.210	0.187	0.209
Sm^{3+}	0.049	0.033	0.082	0.010	0.005	0.006	0.006	0.034	0.023	0.067	0.035	0.016	0.007
Eu^{3+}	0.012	0.009	0.021	0.003	0.002	0.002	0.002	0.010	0.007	0.015	0.010	0.005	0.003
Gd^{3+}	0.019	0.018	0.034	bdl	bdl	bdl	bdl	0.017	0.015	0.030	0.024	0.012	bdl
Th^{4+}	0.002	0.002	bdl	bdl	0.0004	0.001	0.001	0.003	0.002	bdl	bdl	bdl	bdl
CO_3^{2-}	3.997	3.996	6.979	1.001	1.001	1.000	1.002	2.987	2.991	4.962	1.986	1.987	3.992
F^-	3.227	3.267	5.345	1.103	0.022	0.594	1.026	2.184	2.135	3.603	1.076	1.032	bdl
OH^-, calculated					0.977	0.405							
Pr/(Nd+Pr)	0.23	0.23	0.22	0.23	0.25	0.25	0.25	0.22	0.22	0.22	0.21	0.21	0.26

Note: See Online Materials[1] Appendix B for full EPMA data set. bdl = below detectable limit.

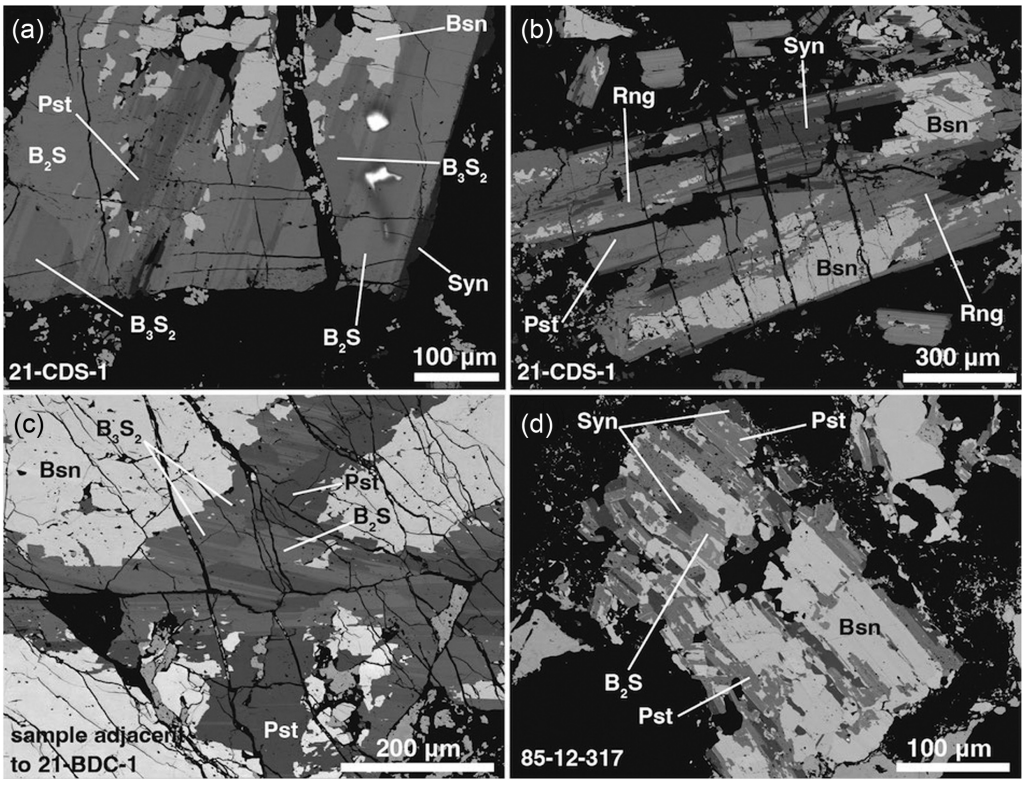

Figure 7. SEM-BSE images of complexly zoned fluorcarbonate minerals from carbonatite dikes north and south of the stock (**a**–**c**) and within the stock (**d**). Different colors correspond to BSE intensities and distinguish different phases. The lightest gray areas correspond to bastnäsite (Bsn). Darker gray areas are composed of the following Ca-REE fluorcarbonates in syntaxial relationship: B_2S, B_3S_2, parisite (Pst), röntgenite (Rng), and synchysite (Syn). Note that intermediate compositional domains may overlap with known B_2S, B_3S_2 compositions as a result of polysomatic faults at the nanoscale. White patches on the right side of phenocryst shown in (**a**) are the result of charging effects.

metals (Ca^{2+} and Sr^{2+}) coordinated to 7 or 8 oxygens in neighboring CO_3^{2-} layers (Ni et al. 1993). Incorporation of heavier REE^{3+} could be accommodated by the different coordination geometry of Ca^{2+} in vaterite layers or distortions of the REE-site caused by the presence of Ca^{2+} (Wall 2000).

Interpretations of Diverse Processes in REE Carbonate Formation

Porphyritic, euhedral, and zoned REE fluorcarbonate mineral textures in the carbonatite dikes support igneous formation, and the evolution from bastnäsite cores to more Ca-rich parisite and synchysite rims may be analogous to zoning of phenocrysts in silicate melts (e.g., plagioclase solid solution, $CaAl_2Si_2O_8$-$NaAlSi_3O_8$). The inability of the system $CeFCO_3$-$CaCO_3$ to form solid solutions results in the formation of complex syntaxial intergrowths (Donnay and Donnay 1953; Ciobanu et al. 2022), rather than the more concentric and gradational zoning typical of silicate phenocrysts. Although many carbonatite intrusions contain early crystallizing (often ephemeral) Na-Sr-Ba-REE carbonate minerals, such as burbankite and carbocernaite (e.g., Bear Lodge and Bears Paw alkaline complexes, U.S.A.; Khibina and Vuoriyarvi complexes, Russia), we have not found any evidence of these minerals at Mountain Pass. Sodium may have been lost to wall-rock fenitization and crystallization of magnesioriebeckite throughout portions of the carbonatite stock and gneiss host rock (Castor 2008).

Carbonatite melts typically become progressively enriched in alkalis, H_2O, sulfate, and fluoride through fractional crystallization, which depresses the solidus and can cause the system to evolve into a carbohydrothermal fluid or brine-melt stage (Anenburg et al. 2021; Yaxley et al. 2022). Jones and Wyllie (1983) found that the solidus temperatures of Mountain Pass carbonatite were near 543 °C and could be further depressed with the addition of volatile components. Based on qualitative and quantitative fluid-mineral stability diagrams constructed by Williams-Jones and Wood (1992) and Gysi and Williams-Jones (2015), the observed phenocryst zoning may be due to changes in the chemical activities ($a\mathrm{Ca}^{2+}$, $a\mathrm{CO}_3^{2-}$, $a\mathrm{REE}^{3+}$, $a\mathrm{F}^-$) and temperatures of carbonatite melt(s) and their evolved/exsolved aqueous fluid(s).

An alternative model to explain the observed fluorcarbonate zoning is through alteration of bastnäsite phenocrysts by late-stage hydrothermal fluid(s) to become enriched in $CaCO_3$ according to the reaction:

$$2\mathrm{REECO_3F} + \mathrm{CaCO_3} = \mathrm{REE_2Ca(CO_3)_3F_2}. \quad (1)$$

Ciobanu et al. (2022) show that mixed-layer series of this type can accommodate superimposed stages of mineralization via nanoscale (re)-equilibration, and that in the bastnäsite-synchysite series, intergrowths can record chemical modulations toward intermediate members in a stepwise approach toward thermodynamic equilibrium.

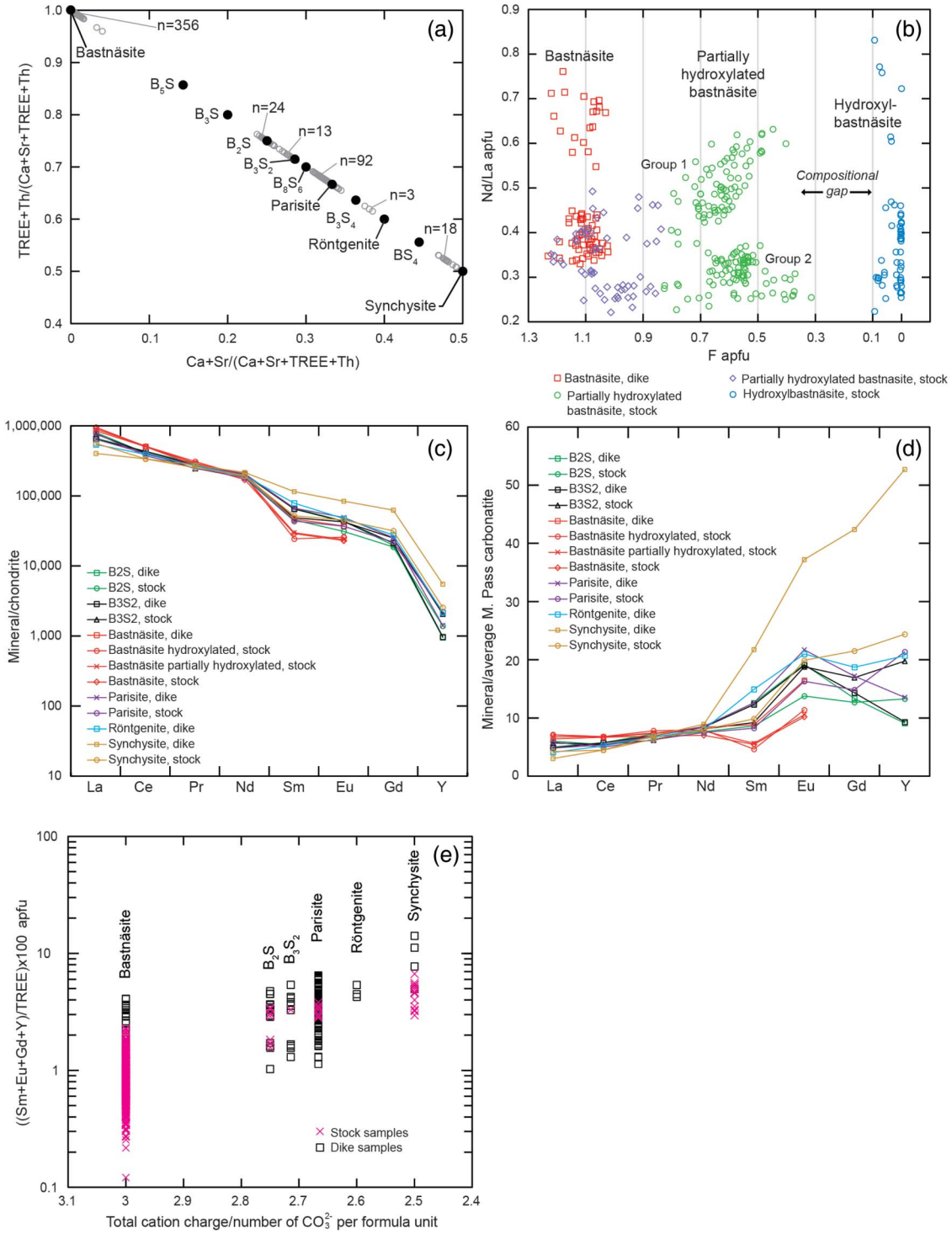

Figure 8. (**a**) Range of REE fluorcarbonate compositions on plot of TREE+Th/total cation content vs. Ca+Sr/total cation content. Intermediate compositional domains that appear to deviate from (and overlap) ideal parisite and polysomes B_2S and B_3S_2, may be due to compositional faults. (**b**) Plot of Nd/La vs. F content in apfu for bastnäsite-hydroxylbastnäsite analyses. (**c**) Chondrite-normalized REE patterns for representative fluorcarbonate compositions. Values below detection are not plotted. (**d**) Fluorcarbonate compositions normalized to an average carbonatite composition from Table 3. Values below detection are not plotted. (**e**) Range of (Sm+Eu+Gd+Y)/TREE × 100 for fluorcarbonates with increasing Ca content, expressed as total cation charge/number of CO_3^{2-} per formula unit.

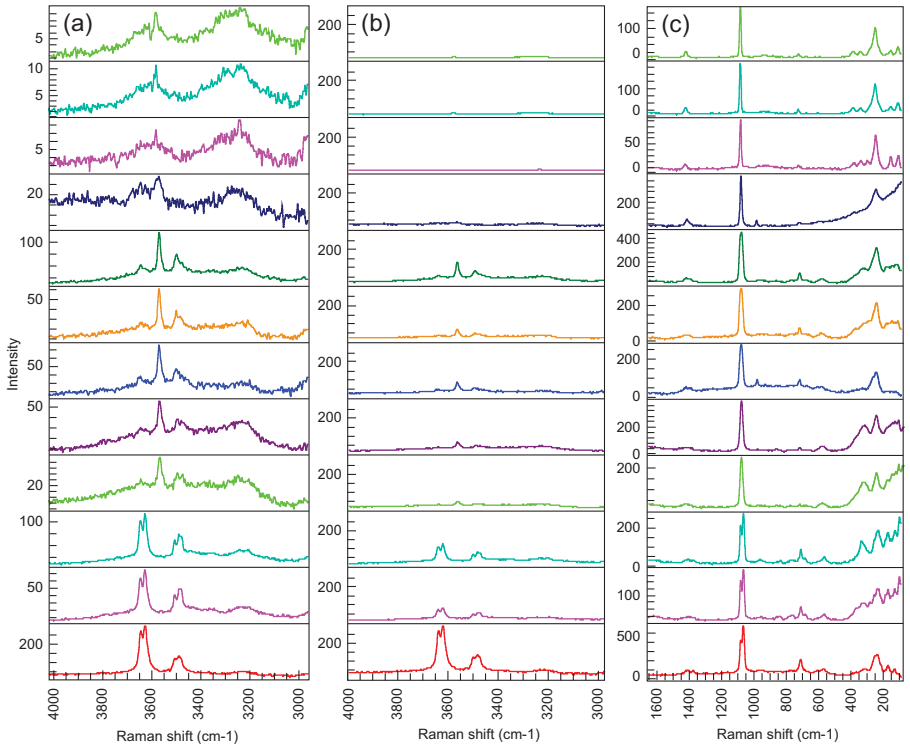

Sample	Mineral	Source
21-BDC-1	Bastnäsite	Dike
21-BDC-1	Bastnäsite	Dike
21-BDC-1	Bastnäsite	Dike
85-9-59	Partially hydroxylated bastnäsite	Stock
17-MP-04H-1	Partially hydroxylated bastnäsite	Stock
17-MP-04H-1	Partially hydroxylated bastnäsite	Stock
17-MP-04H-1	Partially hydroxylated bastnäsite	Stock
85-9-59	Partially hydroxylated bastnäsite	Stock
85-9-59	Partially hydroxylated bastnäsite	Stock
Compositional gap; $P\bar{6}2c$ to $P\bar{6}$ transformation?		
85-5-171	Hydroxylbastnäsite	Stock
85-5-171	Hydroxylbastnäsite	Stock
85-5-171	Hydroxylbastnäsite	Stock

Figure 9. Raman spectra of bastnäsite and hydroxylbastnäsite varieties. (**a**) Spectra showing characteristic bands in the OH^- stretching region (3200–3650 cm^{-1}); rescaled intensity with all spectra occupying an equal Y-axis. (**b**) The same OH^- stretching region plotted with every spectrum on a common Y-axis, highlighting the prominence of OH^- bands for end-member hydroxylbastnäsite. (**c**) Spectra showing characteristic bands in the range 100 to 1600 cm^{-1}.

Though the hydrothermal model is plausible, textural evidence supports the former magmatic model. Abundant fractures bisect tabular bastnäsite phenocrysts at nearly right angles to precursor Ca-rich rim zoning and intergrowth development (e.g., Fig. 7b). Ca-zoning does not correlate with the presence of fractures. If the phenocrysts were altered to Ca-rich fluorcarbonates by late-stage hydrothermal fluids infiltrating solidified carbonatite rocks, it would be expected that the fractures would act as fluid pathways and that the fluorcarbonate crystal domains would therefore be enriched in Ca along fractures. For example, Sr does appear to follow these fractures and veins; celestine cuts across entire bastnäsite phenocrysts (e.g., Fig. 6g). This is consistent with alteration by late-stage, Sr-rich fluids, whereas Ca-rich domains of fluorcarbonate minerals are restricted to what appear to be primary grain boundaries and do not correlate with fractures (e.g., Fig. 6b, 7b, and 7d).

Although some bastnäsite in the carbonatite stock could be primary, occurring as large (>1 mm), euhedral crystals (e.g., Fig. 6f), the prevailing texture is fine-grained (<300 µm) and interstitial to baryte, dolomite, and calcite phenocrysts (e.g., Fig. 6d). Bastnäsite forms pseudomorphic rims with celestine on baryte phenocrysts (e.g., Fig. 6d) and is intergrown with celestine in the groundmass (e.g., Fig. 6e). Celestine appears to be one of the dominant hydrothermal minerals in the carbonatite stock, occurring as veins that crosscut the entire fabric of the rock (e.g., Fig. 6a), including bastnäsite crystals (e.g., Fig. 6g). Secondary calcite veins are also common, some with tiny bastnäsite crystals that either precipitated from fluid or were mechanically removed from the rock during fracturing and brecciation (e.g., Fig. 6f). Secondary veins of sahamalite were found in one thin section (e.g., Fig. 6e). Chemical maps show that in some carbonatite microbreccias, bastnäsite forms the thin matrix lining between carbonatite clasts (Fig. 6h). The combination of these features supports late-stage, interstitial crystallization of bastnäsite in the carbonatite magma followed by crystallization of bastnäsite and hydroxylbastnäsite by aqueous fluids during and after carbonatite solidification. Partially hydroxylated bastnäsite likely resulted from OH^- substituting for F^- (Fig. 8b).

Economic Considerations

Though different REEs have been in demand at different times in the mining history of the Mountain Pass deposit (e.g., Eu as a color phosphor in television sets, Ce as a glass polishing agent, La as an oil refinery catalyst), the current economic driver is Pr+Nd for high field strength magnets. Finished magnet material has an ideal proportion of Pr and Nd, which is monitored upstream using the oxide ratio of $Pr_6O_{11}/(Pr_6O_{11}+Nd_2O_3) \times 100$ in ore, flotation plant concentrate, and leach solutions (E. McNew, MP Materials, written communication 2025). Values maintain consistency at 25 ± 2% and are often observed at the upper levels of this range, which is somewhat a function of ore mineralogy and TREO grade. (E. McNew, MP Materials, written communication 2025). A positive correlation between TREO grade and $Pr/(Nd+Pr) \times 100$ is consistent with bastnäsite as the main control on REE content

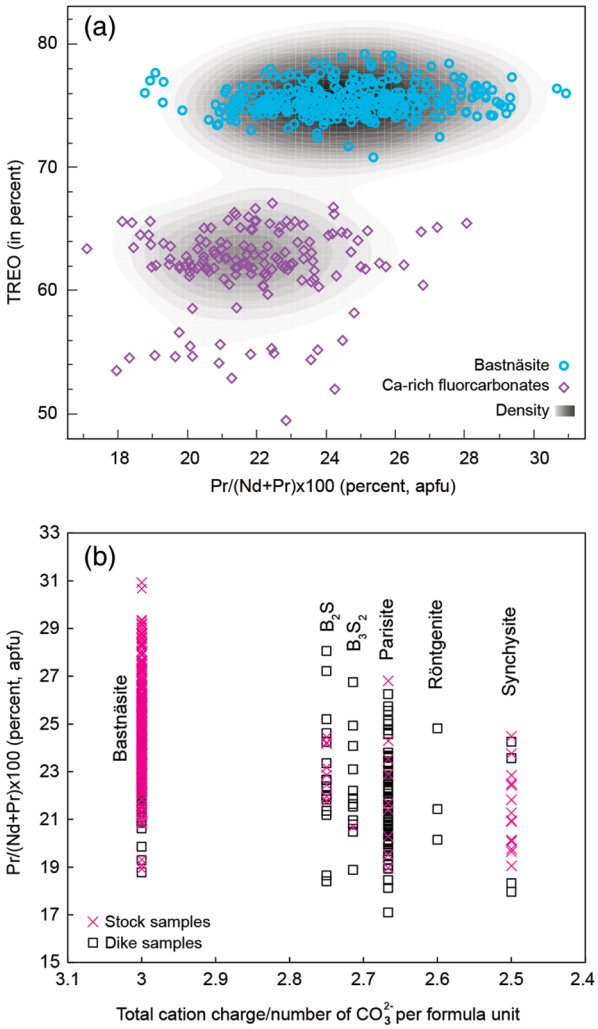

Figure 10. (**a**) Plot of TREO vs. Pr/(Nd+Pr) × 100 for bastnäsite-hydroxylbastnäsite and Ca-REE fluorcarbonates (TREO does not include Y). (**b**) Plot of Pr/(Nd+Pr) × 100 for each fluorcarbonate type with increasing Ca content, expressed as total cation charge/number of CO_3^{2-} per formula unit.

(Fig. 10). Ca-rich fluorcarbonate minerals parisite and synchysite have lower average Pr/(Nd+Pr) × 100 of 22 ± 2% (1 St. dev., n = 147) relative to bastnäsite at 25 ± 2% (1 std dev., n = 355) (Table 4). Bastnäsite incorporates greater proportions of La+Ce and lower Nd concentrations than the Ca-rich fluorcarbonates (Figs. 8c–8d). With little to no difference in Pr content, the Pr/(Nd+Pr) values are higher in bastnäsite. Because different REE fluorcarbonate minerals are characterized by different REE patterns and Pr/(Nd+Pr) × 100, it is possible that ore containing variable bastnäsite:parisite could be mixed to achieve optimal REE grades and Pr/Nd ratios. In contrast with bastnäsite, the Ca-rich fluorcarbonates also contain a larger proportion of higher atomic number REE (Sm, Eu, Gd) and Y relative to total REE (e.g., Figs. 8c–8e). Should market forces increase the demand for higher atomic number REEs, operations could target rock with greater parisite content, though total REE grades would be lower compared to pure bastnäsite ore.

Implications

Our detailed textural and chemical study of carbonate ore minerals points to complex processes of REE mineralization to form the Mountain Pass deposit. Though evidence for primary igneous crystallization is observed, particularly in the carbonatite dikes, late-stage fluids were more important than previously recognized or described. Evolution of a carbonatite melt to a carbohydrothermal fluid (or brine-melt) may have promoted crystallization of Ca-rich fluorcarbonates over bastnäsite, impacting grade, concentration, and inter-element ratios of REEs. Recognition that Ca-rich fluorcarbonate phases (parisite, B_2S, B_3S_2, and synchysite) are likely to contain greater concentrations of mid- and high-atomic number REEs may be important to mining operations. Hydrothermal processes of REE mineralization in the stock are evident by cross-cutting vein textures, brecciation, and hydroxylation of bastnäsite to partial and near end-member hydroxylbastnäsite. Characterizing Mountain Pass ore as bastnäsite is an oversimplification of a carbonatite deposit that contains at least four REE-bearing carbonate mineral species and two intermediate compositions with mixed-layer structures. Atomic-scale investigation of the mineral bonding structures that allow for relatively higher HREE to LREE proportions in Ca-rich fluorcarbonates would augment understanding of ore genesis. The demand for REEs in the Mountain Pass deposit has continued since its discovery, and though the elements of economic interest have changed through time, the unique properties of REEs have enabled diverse technological advances throughout history that will undoubtedly continue into the future, and for applications not yet conceived.

Acknowledgments and Funding

We are grateful to Steve Castor for sharing drill core samples and knowledge of the Mountain Pass REE deposit. Robby Ruesch, Lin Xia, and Nicole Franco of MP Materials provided access to the Mountain Pass mine site. We thank Ed McNew of MP Materials for insightful conversations about Mountain Pass ore and comments on the manuscript draft. Erin Benson, Todd Hoefen, and Jake Poletti of the USGS are acknowledged for helpful scientific discussions about Mountain Pass REE carbonate minerals. Heather Lowers, Andrea Foster, Dawn Ruth, Heather Parks, John Wallis, and Sean Jaramillo of the USGS provided analytical and technical assistance. USGS interns Travis Morton and Zach Shimp assisted in field work and electron microprobe data collection. We thank Jake Poletti, Michael Anenburg, and an anonymous reviewer for their thorough reviews and constructive comments. This research was funded by the USGS Mineral Resources Program. Any use of trade, firm, or product names is for descriptive purposes only and does not imply endorsement by the U.S. Government.

References Cited

Andersen, A.K., Clark, J.G., Larson, P.B., and Donovan, J.J. (2017) REE fractionation, mineral speciation, and supergene enrichment of the Bear Lodge carbonatites, Wyoming, USA. Ore Geology Reviews, 89, 780–807, https://doi.org/10.1016/j.oregeorev.2017.06.025.

Andersen, A.K., Larson, P.B., and Cosca, M.A. (2019) C-O stable isotope geochemistry and 40Ar/39Ar geochronology of the Bear Lodge carbonatite stockwork, Wyoming, USA. Lithos, 324-325, 640–660, https://doi.org/10.1016/j.lithos.2018.11.030.

Anenburg, M., Broom-Fendley, S., and Chen, W. (2021) Formation of rare earth deposits in carbonatites. Elements, 17, 327–332, https://doi.org/10.2138/gselements.17.5.327.

Benson, E.K. and Watts, K.E. (2024) Apatite and monazite geochemistry record magmatic and metasomatic processes in rare earth element mineralization at Mountain Pass, California. Economic Geology and the Bulletin of the Society of Economic Geologists, 119, 1611–1642, https://doi.org/10.5382/econgeo.5108.

Benson, E.K., Watts, K.E., and Hillenbrand, I.W. (2025) 2025, Geochemistry and radiogenic isotopes constrain the mantle source region of the Mountain Pass Intrusive Suite, California. Lithos, 508–509, 108060, https://doi.org/10.1016/j.lithos.2025.108060.

Capitani, G. (2019) HRTEM investigation of bastnäsite–parisite intergrowths from Mount Malosa (Malawi): Ordered sequences, polysomatic faults, polytypic disorder, and a new parisite-(Ce) polymorph. European Journal of Mineralogy, 31, 429–442, https://doi.org/10.1127/ejm/2019/0031-2824.

——— (2020) Synchysite-(Ce) from Cinquevalli (Trento, Italy): Stacking disorder and the polytypism of (Ca,REE)-fluorcarbonates. Minerals, 10, 77, https://doi.org/10.3390/min10010077.

Castor, S.B. (2008) The Mountain Pass rare-earth carbonatite and associated ultrapotassic rocks, California. Canadian Mineralogist, 46, 779–806, https://doi.org/10.3749/canmin.46.4.779.

Ciobanu, C.L., Kontonikas-Charos, A., Slattery, A., Cook, N.J., Ehrig, K., and Wade, B.P. (2017) Short-range stacking disorder in mixed-layer compounds: A HAADF STEM study of bastnäsite-parisite intergrowths. Minerals, 7, 227.

Ciobanu, C.L., Cook, N.J., Slattery, A.D., Ehrig, K., and Liu, W.Y. (2022) Nanoscale intergrowths in the bastnäsite–synchysite series record transition toward thermodynamic equilibrium. MRS Bulletin, 47, 250–257, https://doi.org/10.1557/s43577-022-00318-1.

Conconi, R., Fumagalli, P., and Capitani, G. (2023) A multi-methodological study of the bastnäsite-synchysite polysomatic series: Tips and tricks of polysome identification and the origin of syntactic intergrowths. American Mineralogist, 108, 1658–1668, https://doi.org/10.2138/am-2022-8678.

Conconi, R., Gentile P., Fumagalli, P., Nieto, F., and Capitani, G. (2025) CaREE-fluorcarbonates: A variety of morphologies, compositions and nanostructures with insights into REE partitioning and mobility. Lithos, 504-505, 108033, https://doi.org/10.1016/j.lithos.2025.108033.

Donnay, G. and Donnay, J.D.H. (1953) The crystallography of bastnaesite-(Ce), parisite-(Ce), roentgenite-(Ce) and synchysite-(Ce). American Mineralogist, 38, 932–963.

Donovan, J.J., Snyder, D.A., and Rivers, M.L. (1993) An improved interference correction for trace element analysis. Microbeam Analysis, 2, 23–28.

Donovan, J.J., Singer, J.W., and Armstrong, J.T. (2016) A new EPMA method for fast trace element analysis in simple matrices. American Mineralogist, 101, 1839–1853, https://doi.org/10.2138/am-2016-5628.

Donovan, J.J., Allaz, J.M., von der Handt, A., Seward, G.G.E., Neill, O., Goemann, K., Chouinard, J., and Carpenter, P.K. (2021) Quantitative WDS compositional mapping using the electron microprobe. American Mineralogist, 106, 1717–1735, https://doi.org/10.2138/am-2021-7739.

Frost, R.L. and Dickfos, M.J. (2007) Raman spectroscopy of halogen-containing carbonates. Journal of Raman Spectroscopy, 38, 1516–1522, https://doi.org/10.1002/jrs.1806.

Gysi, A.P. and Williams-Jones, A.E. (2015) The thermodynamic properties of bastnäsite-(Ce) and parisite-(Ce). Chemical Geology, 392, 87–101, https://doi.org/10.1016/j.chemgeo.2014.11.001.

Hornig-Kjarsgaard, I. (1998) Rare earth elements in Sövitic carbonatites and their mineral phases. Journal of Petrology, 39, 2105–2121, https://doi.org/10.1093/petroj/39.11-12.2105.

Jaffe, H.W., Meyrowitz, R., and Evans, H.T. Jr. (1953) Sahamalite, a new rare earth carbonate mineral. American Mineralogist, 38, 741–754.

Jones, A.P. and Wyllie, P.J. (1983) Low-temperature glass quenched from a synthetic, rare earth carbonatite: Implications for the origin of the Mountain Pass Deposit, California. Economic Geology and the Bulletin of the Society of Economic Geologists, 78, 1721–1723, https://doi.org/10.2113/gsecongeo.78.8.1721.

Kamenetsky, V.S., Doroshkevich, A.G., Elliott, H.A., and Zaitsev, A.N. (2021) Carbonatites: Contrasting, complex, and controversial. Elements, 17, 307–314, https://doi.org/10.2138/gselements.17.5.307.

Le Maitre, R.W., Bateman, P., Dudek, A., Keller, J., Lameyre, J., Le Bas, M.J., Sabine, P.A., Schmid, R., Sorensen, H., Steckeisen, A., Woolley, A.R., and Zanettin, B. (1989) A classification of igneous rocks and glossary of terms. Recommendations of the International Union of Geological Sciences on the Systematics of Igneous Rocks, 193 p. Blackwell.

Liu, S.L., Ma, L., Zou, X., Fang, L., Qin, B., Melnik, A.E., Kirscher, U., Yang, K.-F., Fan, H.-R., and Mitchell, R.N. (2023a) Trends and rhythms in carbonatites and kimberlites reflect thermo-tectonic evolution of Earth. Geology, 51, 101–105, https://doi.org/10.1130/G50775.1.

Liu, S.-L., Fan, H.-R., Liu, X., Meng, J., Butcher, A.R., Yann, L., Yang, K.-F., and Li, X.-C. (2023b) Global rare earth elements project: New developments and supply chains. Ore Geology Reviews, 157, 105428, https://doi.org/10.1016/j.oregeorev.2023.105428.

Mariano, A.N. (1989) Nature of economic mineralization in carbonatites and related rocks. In K. Bell, Ed., Carbonatites: Genesis and Evolution, p. 149–176. Unwin Hyman Inc.

McDonough, W.F. and Sun, S. (1995) The composition of the Earth. Chemical Geology, 120, 223–253, https://doi.org/10.1016/0009-2541(94)00140-4.

Meng, D., Wu, X., Mou, T., and Li, D. (2001a) Determination of six new polytypes in parisite-(Ce) by means of high-resolution electron microscopy. Mineralogical Magazine, 65, 797–806, https://doi.org/10.1180/0026461016560010.

——— (2001b) Microstructural investigation of new polytypes of parisite-(Ce) by high-resolution transmission electron microscopy. Canadian Mineralogist, 39, 1713–1724, https://doi.org/10.2113/gscanmin.39.6.1713.

Nassar, N.T. and Fortier, S.M. (2021) Methodology and technical input for the 2021 review and revision of the U.S. Critical Minerals List. U.S.G.S. Open-File Report, Volume 2021–1045, https://doi.org/10.3133/ofr20211045.

Ni, Y., Hughes, J.M., and Mariano, A.N. (1993) The atomic arrangement of bastnäsite-(Ce), Ce(CO3)F, and structural elements of synchysite-(Ce), rontgenite-(Ce), and parisite-(Ce). American Mineralogist, 78, 415–418.

Olson, J.C., Shawe, D.R., Pray, L.C., and Sharp, W.N. (1954) Rare-earth mineral deposits of the Mountain Pass district, San Bernardino County, California. U.S. Geological Survey Professional paper, Volume 261. U.S. Geological Survey.

Poletti, J.E., Cottle, J.M., Hagen-Peter, G.A., and Lackey, J.S. (2016) Petrochronological constraints on the origin of the Mountain Pass ultrapotassic and carbonatite intrusive suite, California. Journal of Petrology, 57, 1555–1598, https://doi.org/10.1093/petrology/egw050.

Sun, S. and McDonough, W.F. (1989) Chemical and isotopic systematics of oceanic basalts: Implications for mantle composition and processes. Special Publication - Geological Society of London, 42, 313–345, https://doi.org/10.1144/GSL.SP.1989.042.01.19.

Taylor, S.R. and McLennan, M. (1981) The composition and evolution of the continental crust: Rare earth element evidence from sedimentary rocks. Philosophical Transactions of the Royal Society of London Series A, 301, 381–399, https://doi.org/10.1098/rsta.1981.0119.

Van Landuyt, J. and Amelinckx, S. (1975) Multiple beam direct lattice imaging of a new mixed-layer compound of the bastnaesite-synchysite series. American Mineralogist, 60, 351–358.

Verplanck, P.L., Mariano, A.N., and Mariano, A.N. Jr. (2016) Rare earth element ore geology of carbonatites. Reviews in Economic Geology, 18, 5–32, https://doi.org/10.5382/Rev.18.01.

Wall, F. (2000) Mineral chemistry and petrogenesis of rare earth-rich carbonatites with particular reference to the Kangankunde carbonatite, Malawi, 284 p. Ph.D. dissertation. University of London.

Watts, K.E. and Andersen, A.K. (2025) Mineral chemistry data for carbonates from the Mountain Pass rare earth element deposit, California: U.S. Geological Survey data release, https://doi.org/10.5066/P1DVJ92S.

Watts, K.E., Haxel, G.B., and Miller, D.M. (2022) Temporal and petrogenetic links between Mesoproterozoic alkaline and carbonatite magmas at Mountain Pass, California. Economic Geology and the Bulletin of the Society of Economic Geologists, 117, 1–23, https://doi.org/10.5382/econgeo.4848.

Watts, K.E., Miller, D.M., and Ponce, D.A. (2024) Mafic alkaline magmatism and rare earth element mineralization in the Mojave Desert, California: The Bobcat Hills connection to Mountain Pass. Geochemistry, Geophysics, Geosystems, 25, e2023GC011253.

Williams-Jones, A.E. and Wood, S.A. (1992) A preliminary petrogenetic grid for REE fluorcarbonates and associated minerals. Geochimica et Cosmochimica Acta, 56, 725–738, https://doi.org/10.1016/0016-7037(92)90093-X.

Wu, X.L., Meng, D.W., Pan, Z.L., Yang, G.M., and Li, D.X. (1998) Transmission electron microscopic study of new, regular, mixed-layer structures in calcium–rare-earth fluorcarbonate minerals. Mineralogical Magazine, 62, 55–64, https://doi.org/10.1180/002646198547468.

Yang, H., Dembowski, R.F., Conrad, P.G., and Downs, R.T. (2008) Crystal structure and Raman spectrum of hydroxyl-bastnäsite-(Ce), $CeCO_3(OH)$. American Mineralogist, 93, 698–701, https://doi.org/10.2138/am.2008.2827.

Yaxley, G.M., Anenburg, M., Tappe, S., Decree, S., and Guzmics, T. (2022) Carbonatites: Classification, sources, evolution, and emplacement. Annual Review of Earth and Planetary Sciences, 50, 261–293, https://doi.org/10.1146/annurev-earth-032320-104243.

Manuscript received March 12, 2025
Manuscript accepted June 15, 2025
Accepted manuscript online June 25, 2025
Manuscript Handled by Nolwenn Coint

Endnotes:

[1]Deposit item AM-26-19822. Online Materials are free to all readers. Go online, via the table of contents or article view, and find the tab or link for supplemental materials.